Review

Determination of pore size and pore size distribution
1. Adsorbents and catalysts

Katsumi Kaneko*

Department of Chemistry, Faculty of Science, Chiba University, 1-33 Yayoi, Inage, Chiba, 263 Japan

Abstract

Various kinds of pores in solid materials are classified into intraparticle pores and interparticle pores according to the origin of the pores. The structural factors of the pores are discussed as well as the methods for evaluation of the pore size distribution with molecular adsorption (molecular resolution porosimetry), small angle X-ray scattering, mercury porosimetry, nuclear magnetic resonance, and thermoporosimetry. Recent progresses in molecular resolution porosimetry for micropores are stressed; this review describes new approaches such as high resolution N_2 adsorption, He adsorption at 4.2 K, and molecular simulation for the characterization of porous solids.

Keywords: Pore size; Pore size distribution; Micropore; Physical adsorption; Micropore field; Small angle X-ray scattering; Surface characterization

Contents

* Corresponding author. Tel.: 81-43-290-2779 (office room);
  Fax: 81-43-290-2788 (office room.)

1. Introduction

Hopefully, human society can benefit by the establishment of better adsorption, separation, and reaction processes. Adsorption and separation can concentrate precious materials and remove pollutants, which are strongly associated with energy and environmental technologies. Excellent adsorbents and membranes are indispensable to realize better adsorption and separation processes. Also highly efficient and selective catalysts can save energy and resources to produce useful materials. Pores lead not only to greater surface area, but also to high selectivity in reaction and adsorption. For example, abundant supercritical NO can be adsorbed in pores of iron oxide-dispersed activated carbon in the form of the dimer; the dimerized NO molecules change into N_2 through N_2O in the presence of SO_2, which suggests a marked acceleration of the high pressure reaction by the pore field [1–6]. Thus, porous solids have gathered much attention from the viewpoint mentioned above. The international symposium on Characterization of Porous Solids (COPS) has been organized every three years [7–9]. The continuity of this symposium provides evidence of the importance of porous solids. Also many clay minerals have been used as representative porous solid systems and their pore structures have been actively studied for the purpose of development of new technologies [10–13]. Furthermore, elucidation of porous structures and chemical properties of minerals and clays can contribute to progress in the earth science and is helpful to preserve the environment of our earth. Pores play an essentially important role in physical and chemical properties of not only adsorbents and catalysts, but also the earth surface.

Do we understand sufficiently the structure and function of pores? Unfortunately they are not fully understood. IUPAC recommended the simple classification of pores such as micropores ($w < 2$ nm), mesopores (2 nm $< w < 50$ nm), and macropores ($w > 50$ nm) according to the pore width w [14]. One hopes to determine the population of pores as a function of the pore width, the so-called pore size distribution, which is the most fundamental information on the pore. However, we must take into account the origin of the pore and we must determine the average three-dimensional geometry of the pore in addition to the one-dimensional pore width. The pore size distribution for mesopores and macropores has been determined by N_2 adsorption and mercury porosimetry. Those porosimetries have assisted to understand the solid properties and develop modern technologies [15,16]. Nevertheless, even N_2 adsorption and mercury porosimetry often show serious disagreement between both evaluations. The relationship between adsorption hysteresis and pore size determination is still an important research problem [17–19]. Assessment of the microporosity is much less-advanced compared to meso- and macropores despite of recent concerns on microporous systems such as zeolites, activated carbons, and clay minerals. Hence, systematic and active research on microporosimetry is really indispensable to design new adsorbents, membranes, and cata-

lysts. In this review, a new classification is proposed with relevance to the origin of pores and recent advances in molecular resolution porosimetry, in particular, on micropores are described.

2. Origin and classification of pores in solid materials

Karnaukhov proposed spongy and corpuscular porous solids, which were morphologically classified [20]. Solid materials, however, have a cohesive structure which depends on the interaction between the primary particles. The cohesive structure leads indispensably to a void space which is not occupied by the composite particles such as atoms, ions, and fine particles. Consequently, the state and population of such voids strongly depends on the interparticle forces. The interparticle forces are different from one system to another; chemical bonding, van der Waals force, electrostatic force, magnetic force, surface tension of adsorbed films on the primary particles, and so on. Even the single crystalline solid which is composed of atoms or ions has intrinsic voids and defects. Therefore, pores in solids are classified into *intraparticle pores* and *interparticle pores* (Table 1).

2.1. Intraparticle pores

2.1.1. Intrinsic intraparticle pore

Zeolites are the most representative porous solids whose pores arise from the intrinsic crystalline structure. Zeolites have a general composition of Al, Si, and O, where Al–O and Si–O tetrahedral units cannot occupy the space perfectly and therefore produce cavities. Zeolites have intrinsic pores of different connectivities according to their crystal structures [21]. These pores may be named *intrinsic crystalline pores*. The carbon nanotube found by Iijima [22] has also an intrinsic crystalline pore; it is a nano carbon fiber having a cylindrical wall. Crysotile $Mg_6Si_4O_{10}(OH)_8$, which is one of the main components of mineral asbestos, has cylindrical pores with a diameter of ~ 7 nm [23]. Although all crystalline solids other than zeolites have more or less intrinsic crystalline pores, these are not so available for adsorption or diffusion due to their isolated state and extremely small size.

There are other types of pores in a single solid particle. α-FeOOH is a precursor material for magnetic tapes, a main component of surface deposits and atmospheric corrosion products of iron-based alloys, and a mineral. The α-FeOOH

Table 1
Classification of pores from origin, pore width w, and accessibility

| *Origin and structure*		
Intraparticle pore	Intrinsic intraparticle pore	Structurally intrinsic type
		Injected intrinsic type
	Extrinsic intraparticle pore	Pure type
		Pillared type
Interparticle pore	Rigid interparticle pore (Agglomerated)	
	Flexible interparticle pore (Aggregated)	
Pore width		
Macropore	$w > 50$ nm	
Mesopore	2 nm $< w < 50$ nm	
Micropore	$w < 2$ nm	
	Supermicropore, $0.7 < w < 2$ nm	
	Ultramicropore, $w < 0.7$ nm	
	(Ultrapore, $w < 0.35$ nm in this review)	
Accessibility to surroundings		
Open pore	Communicating with external surface	
Closed pore	No communicating with surroundings	
Latent pore	Ultrapore and closed pore	

α-FeOOH
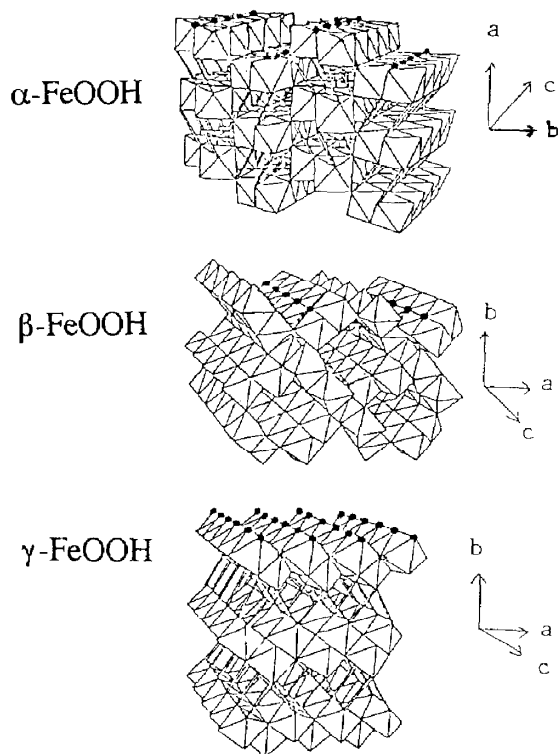
β-FeOOH

γ-FeOOH

Fig. 1. The crystal structures of α-FeOOH, β-FeOOH, and γ-FeOOH.

microcrystal is of thin elongated plate. Fig. 1 shows the crystal structures of three polymorphs of FeOOH. They have their own intrinsic crystalline pores. H_2O molecules are adsorbed in the pore of β-FeOOH, whereas only H_2 can penetrate into the pores between the layers of γ-FeOOH [24]. α-FeOOH has no effective intrinsic pores. α-FeOOH is transformed into α-Fe_2O_3 by heating at 673 K in air; the particle morphology is preserved during the structural transformation, creating pores due to evolution of water [25]. Heat treatment of hydrous zirconia gels changes the porosity due to evolution of water [26]. Thus, *evolution of sublimable chemical substances* introduces pores in solid materials. Sodium silicate glass is widely used in various technologies and occurs in nature. The sodium ions can be easily leached by acid treatment, giving rise to pores. The sodium silicate glass treated by acid shows selective adsorption for ions and gases [27,28]. The *selective dissolution* of some

component creates pores. Activated carbons are the most popular adsorbent [29,30]. Although the origin and mechanism of pore formation in carbons is still actively discussed, basically pores are produced by a *specific reaction* process related to activation. Carbons are mainly composed of micrographitic units. The edge carbon atoms of the micrographite are more reactive than the basal plane carbon atoms, developing pores along the basal plane of the micrographite. A high resolution electron micrograph of activated carbon fiber (ACF) is shown in Fig. 2. The ACF has a relatively uniform pore structure. The pores are distorted slits of 1 nm in width and they are separated by thin graphitic walls.

Thus, modification of intrinsic structures by specific evolution, leaching, and reaction procedures can create pores in solid materials. Also control of defects can be another effective way for pore creation. The van der Waals C_{60} solid has many defects, which form channels. Fig. 3 shows the adsorption isotherm of N_2 on highly defective C_{60} microcrystals at 77 K, which has a sharp initial uptake and shows hysteresis; there are micropores and mesopores (these terms will be explained later) [31,32]. These new created
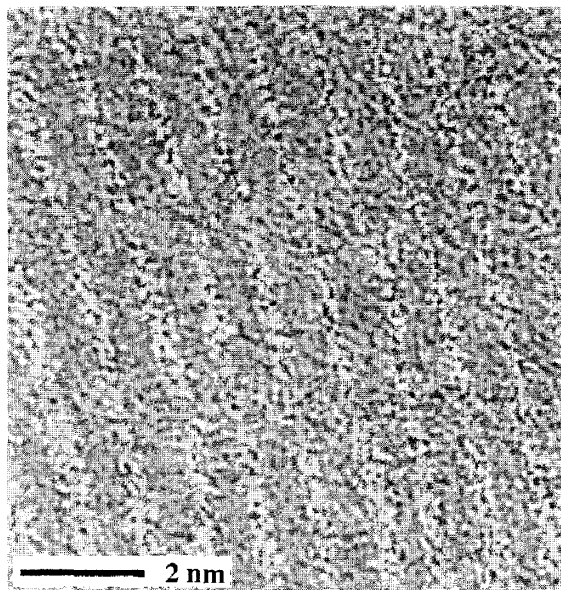

2 nm

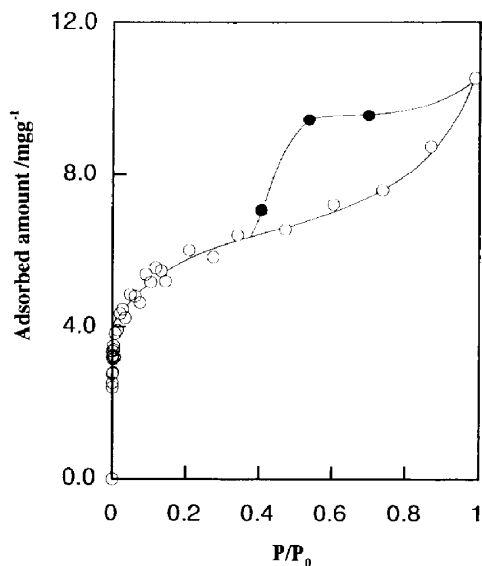Fig. 2. High resolution electron micrograph of activated carbon fiber.

Fig. 3. Adsorption isotherm of N_2 on defective C_{60} crystals: (O) adsorption, (●) desorption.

intrinsic intraparticle pores should have their own name different from the intrinsic intraparticle pore. The latter is called a *structurally intrinsic intraparticle pore*, while the former is called an *injected intrinsic intraparticle pore*.

2.1.2. Extrinsic intraparticle pore

The above-mentioned modification methods can be generally applied to produce porous solids. In this case, a foreign substance is impregnated in the parent material in advance, which is removed by the above modification procedure. For example, Maeda et al. dissolved decomposable substances into the reactant starting material to produce new porous alumina [33]. This type of pores should be called *extrinsic intraparticle pores*. Strictly speaking, as this material does not contain other components, *extrinsic pure intraparticle pore* is recommended. However, the extrinsic intrapore can be regarded as the interparticle pore in some cases.

We can introduce a pore-forming agent into the structure of solids to produce voids or fissures which work as pores. This concept has been applied to layered compounds in which the interlayer bonding is very weak; some inserting substance swells the interlayer space. Graphite is a

representative layered compound; the graphitic layers are weakly bound to each other by the van der Waals force [34]. If we heat it in the presence of intercalants such as K atoms, the intercalants are inserted between the interlayer spaces to form a long periodic structure. K-intercalated graphite can adsorb a great amount of H_2 gas, while the original graphite cannot [35]. The interlayer space opened by intercalation is generally too narrow to be accessed by larger molecules than H_2; Sakuno et al. recently tried to prepare graphite intercalated compounds which have selective adsorption for organic molecules [36]. Intercalation produces not only pores, but also changes the electronic properties. Montmorillonite is a representative layered clay compound, which swells in solution to intricate hydrated ions or even surfactant molecules [37,38]. Then some pillar materials such as metal hydroxides are intricated in the swollen interlayer space under wet conditions. As the pillar compound is not removed upon drying, the swollen structure can be preserved even under dry conditions. The size of pillars can be more than several nm, being different from the above intercalants. Mesoporous kanemites were recently prepared by template and pillar of the surfactant molecular assemblies [39]. As the graphite intercalation compounds and pillar ones need the help of foreign substances, they should be distinguished from the intrinsic intraparticle pore system. Their pores belong to extrinsic intraparticle pores. As the intercalation can be included in the pillar formation, it is better to say that both the pillared and intercalated compounds have *pillared intraparticle pores*.

2.2. Interparticle pores

Primary particles stick together to form a secondary particle, depending on their chemical composition, shape and size. In colloid chemistry, there are two gathering types of primary particles. One is aggregation and the other is agglomeration. The aggregated particles are loosely bound to each other and the assemblage can be readily broken down. Heating or compressing the

assemblage of primary particles brings about the more tightly bound agglomerate.

There are various interaction forces among primary particles, such as chemical bonding, van der Waals force, magnetic force, electrostatic force, and surface tension of the thick adsorbed layer on the particle surface. Sintering at the neck part of primary particles produces stable agglomerates having pores. The aggregate bound by the surface tension of adsorbed water film has flexible pores. Thus, interparticle pores have wide varieties in stability, capacity, shape, and size, which depends on the packing of primary particles. They play an important role in nature and technology regardless of insufficient understanding. The interparticle pores can be divided into *rigid* and *flexible pores*. The stability depends on the surroundings. Almost all interparticle pores in agglomerates are rigid, whereas those in aggregates are flexible. Almost all sintered porous solids have rigid pores due to strong chemical bonding among the particles.

The rigid interparticle porous solids have been widely used and have been investigated as adsorbents or catalysts. Silica gel is a representative of interparticle porous solids. Ultrafine spherical silica particles form the secondary particles, leading to porous solids. Avery and Ramsay showed that the pore of compacted silica varies with the compacting pressure [40]. Recently a carbon gel has been developed, which has great surface area due to interparticle pores [41]. Alunite platelets gather to produce considerably stable aggregates of slit-shaped pores [42]. The oriented aggregate of boehmite platelets has ordered slit-shaped pores of interparticle gaps; their film and plug forms are available [43,44].

3. Structure of pores

The pore state and structure mainly depend on the origin. The pores communicating with the external surface are named *open pores*, which are accessible for molecules or ions in the surroundings. If the porous solids are insufficiently heated, some parts of pores near the outer shell are collapsed inducing *closed pores* without communi-

cation to the surroundings. Closed pores also remain by insufficient evolution of gaseous substance. The closed pore is not associated with adsorption and permeability of molecules, but it influences the mechanical properties of solid materials. Strictly speaking, the new concept of *latent pores* is necessary for the best description of the pore system. This is because the communication to the surroundings often depends on the probe size, in particular, in the case of molecular resolution porosimetry. The open pore with a pore width smaller than the probe molecular size must be regarded as a closed pore. Such effectively closed pores and chemically closed pores should be designated the latent pores [45]. The combined analysis of molecular resolution porosimetry and small angle X-ray scattering (SAXS) offers an effective method for separate determination of open and closed (or latent) pores, which will be described later. The *porosity* is defined as the ratio of the pore volume to the total solid volume; three kinds of densities, true density ρ_t, apparent density ρ_{ap}, and He-replacement density ρ_{He}, can determine the open pore porosity ϕ_{op} ($= 1 - \rho_{ap}/\rho_{He}$) and closed pore porosity ϕ_{cp} [$= \rho_{ap}(1/\rho_{He} - 1/\rho_t)$]. Thus, densities are essentially important. Nevertheless, determination of these densities is not necessarily easy; the true density is given by the unit cell structure with the X-ray diffraction for well-crystalline materials [45,46].

The geometrical structure of pores is of great concern, but the three-dimensional description of pores is not established in less-crystalline porous solids. Only intrinsic crystalline intraparticle pores offer a good description of the structure. The hysteresis analysis of molecular adsorption isotherms and electron microscopic observation estimate the pore geometry such as cylinder (cylinder closed at one end or cylinder open at both ends), cone shape, slit shape, interstice between closed-packing spheres and ink bottle (Fig. 4). However, these models concern with only the unit structures. The higher order structure of these unit pores such as the network structure should be taken into account. The simplest classification of the higher order structures is one-, two-, and three-dimensional pores [47].
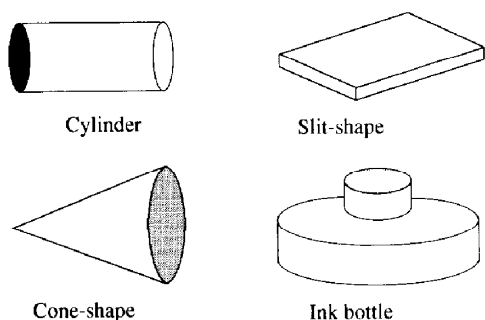
Fig. 4. Pore shapes.

Some zeolites and aluminophosphates have one-dimensional pores, and activated carbons have basically two-dimensional slit-shaped pores with complicated network structures.

There was no clear classification of pores before the following IUPAC recommendation, although macro- and micropores had been used since Russel's classification [48]. The IUPAC has tried to establish a classification of pores according to the pore width (the shortest pore diameter), because the geometry determination of pores is still very difficult and molecular adsorption can lead to the reliable parameter of the pore width w. The pores are divided into three categories: *macropores*, *mesopores*, and *micropores*, as mentioned above. The fact that *nanopores* are often used instead of micropores should be noted. These sizes were determined from the aspect of N_2 adsorption at 77 K, and hence N_2 molecules are adsorbed by different mechanisms – multilayer adsorption, capillary condensation, and micropore filling for macropores, mesopores, and micropores, respectively, as explained later. The critical widths of 50 and 2 nm are chosen from empirical and physical reasons. The pore width of 50 nm corresponds to the relative pressure P/P_0 of 0.96 for the N_2 adsorption isotherm; adsorption experiments above $P/P_0=0.96$ are considerably difficult and applicability of the capillary condensation theory is not sufficiently examined. The smaller critical width of 2 nm corresponds to $P/P_0=0.39$ through the Kelvin equation, where an unstable behavior of the N_2 adsorbed layer (tensile strength effect) is observed; the capillary condensation theory cannot

be applied to pores having a smaller width than 2 nm. The micropores have two subgroups, namely *ultramicropores* ($w<0.7$ nm) and *supermicropores* (0.7 nm $<w<2$ nm). The statistical thickness of the adsorbed N_2 layer on solid surfaces is 0.354 nm. The maximum size of ultramicropores corresponds to the bilayer thickness of nitrogen molecules, and the adsorbed N_2 molecules near the entrance of the pores often block further adsorption. The ultramicropore assessment by N_2 adsorption has an inevitable and serious problem; the micropores are divided into two groups. In this review, the term ultrapore is used for ultramicropores having a width less than 0.35 nm which cannot be accessed by N_2 at 77 K, but by He at 303 K. In addition, He adsorption at 4.2 K was recently proposed for this purpose. Recently the molecular statistical theory has been used to examine the limitation of the Kelvin equation and predicts that the critical width between the micropore and the mesopore is 1.3–1.7 nm (corresponding to 4–5 layers of adsorbed N_2), which is smaller than 2 nm [49,50]. The structure of pores is summarized in Table 1.

4. Molecular resolution porosimetry

Solid surfaces have been characterized by the molecular adsorption theory. In this review, the pore analysis with molecular adsorption is designated as molecular resolution porosimetry; the dynamic method using molecular sieving characteristics will be briefly described later. When high resolution analysis of solid surfaces is requested, the probe molecule must have the necessary requirements of sufficiently small size, stability, easiness of adsorption, and established adsorption theory. N_2 adsorption at 77 K with typical physical adsorption has been devoted to the surface characterization [51]. The effective size of the N_2 molecule on the solid surface is 0.354 nm, and hence the N_2 adsorption can describe the subnano-structure of solid surfaces without chemical destruction. H_2O, Ar, CO_2 and He are also used as probe molecules for the analysis of microporous systems. H_2O and CO_2 have been used for evaluation of the microporosity of hydrophilic zeolites and activated carbons, re-

Table 2
Small probe molecules and adsorption conditions

	He	H_2O	N_2	CO_2
Molecular area (nm^2)	0.117	0.125	0.162	0.142–0.244
Collision diameter (nm)	0.20	0.27	0.41	0.45
Molecular diameter from the van der Waals constant (nm)	0.42	0.46	0.50	0.51
Adsorption temperature (K)	4.2	room temp.	77	room temp.
Interaction	weak	dipole	quadrupole	quadrupole
Adsorbent	any	hydrophilic	any	any

spectively [52]. Table 2 summarizes the properties of these probe molecules and adsorption conditions. Molecular resolution porosimetry cannot only use a single-probe molecule, but also multiprobe molecules having different molecular sizes. The surface fractal analysis using multiprobe molecules is a powerful surface characterization method [53], which can be applied even to the micropore analysis [54]. The multiprobe adsorption method is also very effective for the evaluation of the pore size distribution [55,56]. However, the molecular resolution porosimetry with a single-probe molecule will be mainly described here.

4.1. Molecular adsorption experiment and adsorption isotherms

An adsorption isotherm consists of a series of measurements of the adsorbed amount as a function of the equilibrium gas pressure at a constant temperature. The amount of adsorption (the material adsorbed by the solid is termed the adsorbate) can be determined either gravimetrically or volumetrically after degassing of the sample solids (the adsorbent) above 373 K. The evacuation temperature should be changed according to the surface nature of the sample. The equilibration time must be measured in advance. The commercial adsorption equipment adopts the volumetric method having several advantages such as high sensitivity, low cost and high performance. New volumetric equipment uses highly sensitive pressure gauges such as Baratron gauges instead of mercury. However, the

dead volume correction and maintaining the constant liquid N_2 level should be strictly done in order to get reliable data. If not so, a serious cumulative error of more than 20% is often produced. The gravimetric equipment must have a sensitive balance such as a quartz spring or an electronic balance in addition to the high sensitive pressure gauges. The gravimetric method can determine independently both the adsorbed amount and the equilibrium pressure though the costs are high. The weight changes that occur due to buoyancy as the density of the surrounding adsorptive changes should be corrected. We must subtract the weight of the sample in vacuo from the weight at the adsorption conditions (strictly speaking, it is better to measure the weight change under an adsorptive atmosphere at supercritical conditions without adsorption). The gravimetric adsorption apparatus which can be constructed in each laboratory is shown in Fig. 5. This apparatus automatically determines a high resolution N_2 adsorption isotherm of 50–100 measuring points [57].

The amount of adsorption W_a depends on the gas equilibrium pressure P, adsorption temperature T, adsorptive (gas), and the amount of the adsorbent. The parameters other than P are fixed for measuring the adsorption isotherm and W_a is expressed as a function of P. Physical adsorption is the predominant process for a gas (namely vapor) below the critical temperature, which has the saturated vapor pressure P_o. The pressure is expressed by the relative pressure P/P_o. Here, W_a may be expressed by the mass of gas (usually mg) or the volume reduced to STP [usually cm^3
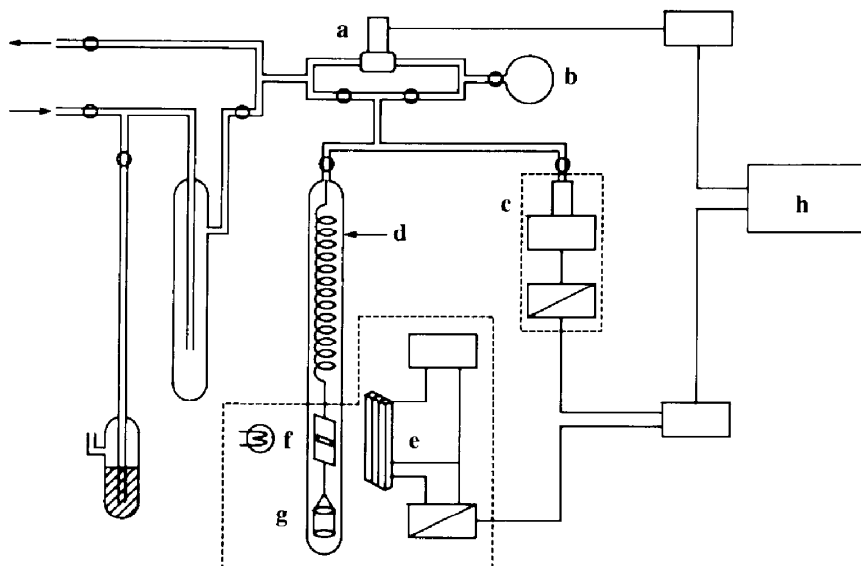
Fig. 5. Schematic diagram of the gravimetric adsorption apparatus. (a) Electromagnetic valve, (b) gas reservoir, (c) pressure sensor, (d) quartz spring, (e) weight sensor, (f) lamp, (g) sample and (h) computer.

(STP)] per unit mass of the adsorbent (usually g). The IUPAC recommended the following six types of the adsorption isotherms instead of the BDDT five groups, as shown in Fig. 6 [14,58]. The type I isotherm corresponds to the so-called Langmuir isotherm. In the case of physical adsorption, the type I isotherm represents presence of micropores where molecules are adsorbed by micropore filling which has been actively studied in adsorption science. The type II isotherm is the most familiar; the multilayer adsorption theory by Brunauer, Emmett, and Teller was originally developed for this type of adsorption [59]. Hence, this isotherm is indicative of the multilayer adsorption process, suggesting the presence of nonporous or macroporous surfaces. Although the adsorption isotherm near $P/P_o = 1$ gives important information on macropores, such an analysis is not practical for accurate measurement. This is because serious condensation on the apparatus walls begins near the saturated vapor pressure. Adsorption from solution using macromolecules has been applied to macropore analysis, but we still need more examinations. Consequently, only macropore analysis with mercury porosimetry is described in this review.
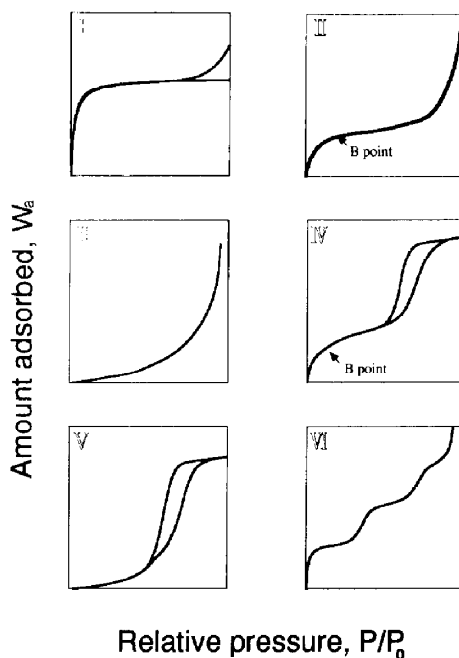

Fig. 6. IUPAC classification of adsorption isotherms.

The type III isotherm arises from nonporous or macroporous surfaces which interact very weakly with the adsorbent molecules. The type IV iso-

therm gives useful information on the mesopore structure through its hysteresis loop, that is, non-overlapping of the adsorption and desorption branches. In the mesopores, molecules form a liquid-like adsorbed phase having a meniscus of which curvature is associated with the Kelvin equation, providing the pore size distribution. The type V isotherm is closed to the type IV isotherm instead of very weak adsorbent–adsorbate interaction. The type VI isotherm is the stepped adsorption isotherm which comes from phase transition of the adsorbed molecular layer or adsorption on the different faces of crystalline solids. In the following description, mainly type I and IV isotherms will appear in relation to the micropore and mesopore analyses, respectively.

4.2. Comparison plots

It is difficult to compare one adsorption isotherm with another, but determination of the deviation from the linearity using a standard adsorption isotherm is easy and accurate. The plot constructed with the aid of standard data is called a comparison plot. The representative comparison plots are the t and α_s plots. The molecular adsorption isotherm on nonporous solids, which can be well described by the BET theory, having a clear B point and similar chemical structure has been used for a standard isotherm. Lippens and de Boer provided a convenient and useful t plot analysis [60]. In the t plot analysis, the adsorbed amount, W_a, of the standard isotherm is converted to the average thickness, t, of adsorbed film with the equation $t = (W_a/W_m)\sigma_t$. Here σ_t is the thickness of a single adsorbed layer (σ_t of N_2: 0.354 nm). Then, P/P_o is transformed into t, so that the abscissa of the t plot is expressed by t instead of P/P_o. If the isotherm under test is also described by the multilayer adsorption, the t plot is a straight line passing through the origin, whose slope is proportional to the surface area. The deviation from the linearity of the t plot gives information on the sort of pores, the average pore size, the surface area, and the pore volume. However, the t plot analysis has the limited applicability to the microporous system due to the absence of explicit monolayer adsorption.

Sing and co-workers proposed a more general comparison plot [61,62]. The ratio of the adsorption at P/P_o to the adsorption at $P/P_o = 0.4$ ($W_{0.4}$) for the standard isotherm, which is designated α_s ($= W_a/W_{0.4}$), is plotted against P/P_o, and the P/P_o axis can then be expressed by α_s. The test isotherm can be replotted with the adsorption W_a against α_s, which is called the α_s plot. The construction of the α_s plot does not need the monolayer capacity, so that it is applicable to microporous solids. The straight line passing the origin guarantees multilayer adsorption, that is, absence of meso- and/or micropores; the deviation leads to valuable information on the pore structures. Kaneko et al. introduced the high resolution α_s analysis using a high resolution standard adsorption isotherm [63,64]. The high resolution α_s analysis determines the plot in a small α_s region below $\alpha_s = 0.7$, which was not originally used for analysis by Sing et al. The high resolution α_s plot has a characteristic feature according to the pore structure. The typical types of the α_s plots are shown in Fig. 7. A nonporous solid has a single line passing the origin, while the line from the origin for the α_s plot of the mesoporous system bends with an upward hump in the α_s region of 0.7 to 1.0. The slopes of the straight line through the origin and the line at the high α_s region gives the total and mesoporous surface areas, respectively. Also the extrapolation of the high α_s region line to the ordinate leads to the mesopore volume. The high resolution α_s
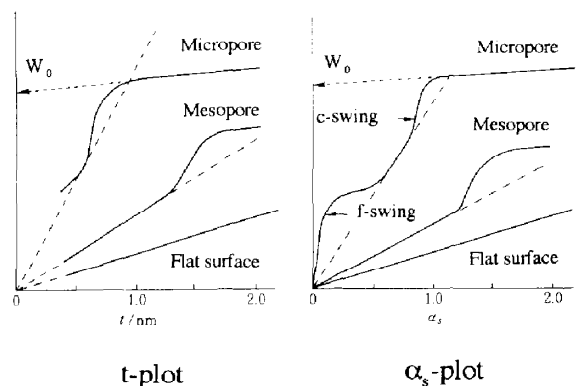

t-plot α_s-plot

Fig. 7. t and α_s plots for adsorption isotherms on flat surface, mesopore, and micropore.

analysis is especially effective for determination of the micropore structure. The α_s plot for a microporous system has one or two upward swings below $\alpha_s = 1.0$. The swing at the lower (f swing) and the higher (c swing) α_s region are designated as the filling and condensation swings, respectively. The type of the α_s plot suggests the presence of ultramicropores and/or supermicropores. Detailed analysis results will be shown for the micropore analysis. The standard α_s and t values for carbonous materials are shown in Table 3. The standard data of similar material to the sample should be used for the construction of the t or α_s plot.

4.3. Mesopore analysis

The adsorbed molecules can produce the liquid layer of the curved meniscus at a lower vapor pressure than the saturated vapor pressure of the bulk liquid, and thereby leads to a marked increase in adsorption below $P/P_o = 1$. Strictly speaking, the liquid layer is formed on the multilayer adsorbed film on the mesoporous surface. The saturated vapor depression of the curved liquid layer can be deduced by the well-known Kelvin equation.

$$\ln(P_r/P_o) = -(2\gamma V_l \cos\theta_c)/(RTr_m) \qquad (1)$$

P_o and P_r represent the saturated vapor pressures of the bulk liquid, which corresponds to

Table 3
The standard N_2 adsorption data for t and α_s plots

P/P_0	α_s	P/P_0	α_s	t (nm)
0.00050	0.244	0.01262	0.490	–
0.00070	0.269	0.01325	0.492	0.281
0.00104	0.293	0.01466	0.499	0.286
0.00155	0.352	0.01589	0.504	0.288
0.00206	0.371	0.01726	0.511	0.292
0.00250	0.382	0.01927	0.518	0.296
0.00275	0.384	0.02089	0.523	0.299
0.00320	0.394	0.02252	0.530	0.303
0.00349	0.398	0.02358	0.534	0.305
0.00426	0.406	0.02571	0.538	0.307
0.00454	0.414	0.04194	0.572	0.327
0.00481	0.423	0.05718	0.599	0.342
0.00513	0.431	0.07407	0.618	0.353
0.00554	0.438	0.08926	0.633	0.362
0.00607	0.442	0.10286	0.656	0.374
0.00670	0.448	0.11564	0.671	0.383
0.00726	0.452	0.12901	0.684	0.390
0.00767	0.445	0.14256	0.705	0.402
0.00796	0.456	0.20834	0.774	0.442
0.00802	0.461	0.27460	0.851	0.486
0.00839	0.463	0.33949	0.931	0.532
0.00888	0.466	0,40582	1.008	0.575
0.00925	0.468	0.47504	1.098	0.627
0.00961	0.471	0.53994	1.189	0.679
0.00976	0.474	0.60304	1.266	0.723
0.00986	0.475	0.66562	1.351	0.772
0.01019	0.477	0.72859	1.441	0.822
0.01063	0.478	0.79301	1.551	0.886
0.01153	0.481	0.85667	1.700	0.971
0.00192	0.485	0.92165	1.893	1.081
0.01231	0.488	0.99668	2.283	1.304

$r_{\rm m}=\infty$ and the curved adsorbed layer, respectively. Here, $r_{\rm m}$ is the mean radius of curvature of the meniscus of liquid formed in the pore. A curved liquid meniscus is expressed by two radii of curvature, r_1 and r_2 ($1/r_1+1/r_2=2/r_{\rm m}$). V_l, γ and $\theta_{\rm c}$ are the molar volume, the surface tension of the liquid and the contact angle, respectively. If there are empty pores corresponding to $r_{\rm m}$ (now neglecting the multilayer adsorption), vapors in the pores condense at the relative pressure of $P_{\rm r}/P_{\rm o}$, leading to a steep increase in the adsorption isotherm. When the pressure is lower, the filled pores will be completely emptied. However, when the curvature of the meniscus of the liquid formed on adsorption does not coincide with that on desorption, hysteresis is observed. Consider the condensation and evaporation of liquid in a cylinder open at both ends with radius r_1. In this case, condensation commences at the pressure, $P_{\rm con}$, corresponding to a flat meniscus formation ($2/r_{\rm m}=1/r_1$), whereas evaporation takes place from the hemispherical meniscus at each end at the pressure, $P_{\rm ev}$, corresponding to $2/r_{\rm m}=2/r_1$. Then $P_{\rm con}>P_{\rm ev}$ with the aid of the Kelvin equation. This discrepancy leads to adsorption hysteresis. De Boer et al. [65], Everett et al. [66] and others studied the relationship between the pore structure and the hysteresis shape. Originally de Boer proposed five types (so-called A, B, C, D, and E) of hysteresis loops. The three types A, B, and E have been used for describing the mesopore geometries. The IUPAC also recommended a new classification of hysteresis loops. These consist of four types shown in Fig. 8 [14]. The IUPAC classification uses the symbols H_1, H_2, H_3, and H_4. Here, H_1, H_2, and H_3 almost correspond to the de Boer's types A, E, and B, respectively. H_4 which has the type I isotherm character is added.
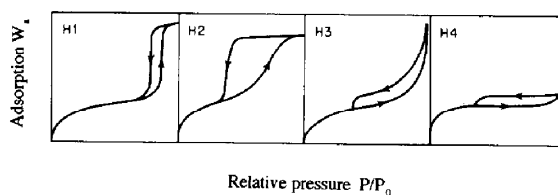
The type H_1 is observed in the case of mesopores having geometries, for example, (1) tubular capillary open at both ends, (2) tubular capillaries with cross sections of two different main dimensions, and (3) narrow-necked ink bottle. The N_2 adsorption isotherm by a single-crystalline zeolite gives this type [67], although the hysteresis is in the lower P/P_0 region. On the other hand, there is no hysteresis in the N_2 adsorption isotherm on MCM-41, although MCM-41 has very uniform cylindrical open mesopores [68]; MCM-41 is a mesoporous zeolite prepared by the template technique using cylindrical micelles of surfactant molecules [69]. The H_2 type is often observed in the adsorption isotherms of silica gel or cracking catalysts, although the pore geometry is not sufficiently fixed. Fundamentally the pore of this type may have the structure similar to the H_1 type, in which there is some size distribution in the narrowed part. There are mainly two cases in which type H_3 can be formed; very wide capillaries having narrow openings and an interstice between the parallel plates. The type H_3 is also found in adsorption isotherms of many crystalline metal oxide aggregates of sheet-like shape. Swollen montmorillonites often show this type; the slit width increases during adsorption and decreases irreversibly during desorption [70]. To some extent microporous carbon with mesopores exhibits type H_4 behavior [71]. In the discussion of the mesopore shape, the contact angle $\theta_{\rm c}$ is assumed to be zero (uniform adsorbed film formation). The lower hysteresis loop of the same adsorbate encloses at a common relative pressure depending to the stability of the adsorbed layer regardless of the different adsorbents due to the so-called tensile strength effect. This tensile strength effect is not sufficiently considered for analysis of mesopore structures [72].

The Kelvin equation provides the relationship between the pore radius and the amount of adsorption at a relative pressure. Many researchers developed a method for the calculation of the pore size distribution on the basis of the Kelvin equation with a correction term for the thickness of the multilayer adsorbed film. The so-called BJH (Barret–Joyer–Halenda) and DH (Dolli-

Fig. 8. IUPAC classification of adsorption hysteresis.

more–Heal) methods have been widely used for such calculations [73,74]. As mathematical details are shown in other articles, only the simple Fortran program for the DH method is described here, Table 4. (This program can be easily used for the analysis of the mesopore size distribution. The thickness correction is done by the Dollimore–Heal equation, $t(nm) = 0.354[5/\ln(P_0/P)]^{1/3}$ [75]). One can calculate the mesopore size distribution for cylindrical or slit-shaped mesopores with this program. The more exact program for the determination of the mesopore size distribution was developed by Morioka [76]. Everett et al. [66] and others [77,78] showed that the pore network effect is serious in the desorption branch, and therefore the determination of the pore size distribution from the adsorption branch was recommended. Also the tensile strength effect should be taken into account in the desorption branch. Therefore, the adsorption branch provides more reliable results. However, the adsorption branch gives a wide distribution compared to the desorption branch due to gradual uptake. Theoretical studies on these points are still done [18,19]. The pore size distribution from the Kelvin equation should be limited to mesopores due to the ambiguity of the meniscus in the microporous region.

4.4. Micropore analysis

Molecular resolution porosimetry must show its effectiveness for micropore analysis. Nevertheless, molecular adsorption mechanisms in micropores is under active discussion. The time is not yet ripe for a molecular resolution analysis in micropores compared to mesopore size distribution analysis, but there has been much progress in this field. The most simple method for the evaluation of the micropore size is the modified Kelvin equation in which the thickness t of the adsorbed layers is taken into account. The t value is obtained from the standard t curve. The modified Kelvin equation indicates that the pressure at which condensation occurs (condensation pressure) is lowered.

$$\ln(P_r/P_0) = -(2\gamma V_l \cos\theta_c)/[RT(r_m - 2t)] \quad (2)$$

However, even the modified Kelvin equation becomes less appropriate for the description of adsorbed layers in molecular-size pores because of no continuous meniscus formation. In the case of the N_2/carbon system, the condensation pressure from the modified Kelvin equation is assumed to be almost twice the theoretical pressure from the molecular simulation even at a pore width of 2.5 nm [49]. Almost all established methods for the mesopore size distribution originate from the modified Kelvin equation, and another analysis should therefore be applied to micropore systems. Here, the average micropore field, a thermodynamic description, α_s analysis, a combined method of the average potential and pore width, and the molecular statistical method will be described.

4.4.1. Average micropore field

In a microporous system, the opposite micropore walls are so closed to each other that the potentials from the surfaces overlap increasing the potential depth, and enhanced adsorption at an extremely low pressure region occurs.

The adsorption of a N_2 molecule on the neutral surface can be approximated by a simple interaction of a spherical molecule with the surface atoms, so that the van der Waals force is considered. The van der Waals interaction between a molecule and a surface atom as a function of the distance r, $\Phi(r)$, can be expressed by the Lennard-Jones potential,

$$\Phi(r) = 4\epsilon_{sf}[(\sigma_{sf}/r)^{12} - (\sigma_{sf}/r)^6] \quad (3)$$

where ϵ_{sf} and σ_{sf} are fitted parameters for the nitrogen–graphitic carbon well depth and effective diameter. These parameters are calculated according to the Lorentz–Berthelot rules: $\epsilon_{sf} = (\epsilon_{ss}/\epsilon_{ff})^{1/2}$; $\sigma_{sf} = (\sigma_{ss} + \sigma_{ff})/2$. Here, $(\sigma_{ss}, \epsilon_{ss})$ and $(\sigma_{ff}, \epsilon_{ff})$ are the Lennard-Jones parameters for solid and fluid(gas) atoms, respectively [78]. Everett and Powl derived the interaction energy between a molecule and two parallel lattice planes for a slit-shaped pore and for a cylindrical pore [79]. For example, the potential Φ_{GR} between a N_2

Table 4
Fortran program for the DH method

```
C               CALCULATION OF THE PORE SIZE DISTRIBUTION
C               BY THE DOLLIMORE–HEAL METHOD.
                REAL P (100), AM (100), RK (100), T (100)
                REAL S, SSC, SSP, L, LL, LM, V, DV, A, B, RM, TM, DT
                INTEGER I, IMAX
                CHARACTER NAME*50
                SSP=0.0
                SSC=0.0
                LL=0.0
C               P...RELATIVE PRESSURE: AM...AMOUNT OF ADSORBED
C               T...THICKNESS OF ADSORBED N2 LAYER
C               RK...RADIUS CALCULATED BY KELVIN EQ.
                WRITE (*,*) 'CALCULATION OF PORE SIZE DISTRIBUTION BY
                +DOLLIMORE–HEAL METHOD'
                WRITE (*,*) ''
                WRITE (*,*) 'PLEASE INPUT THE DATA FILE NAME?'
                READ (*,101) NAME
                OPEN (1, FILE=NAME, STATUS='OLD')
C               RELATIVE PRESSURE AMOUNT OF ADSORBED (ML/G)
                DO 10 I=1 TO 99
                READ (1, *, END=99) P(I), AM(I)
                IMAX=I
        10      CONTINUE
        99      CONTINUE
                CLOSE (1, STATUS='KEEP')
C               CALCULATION OF PORE RADIUS AND THICKNESS OF N2 LAYER
                DO 20 I=1, IMAX
                RK (I)=−0.953/LOG (P(I))
                T(I)=0.354*(−5.0/LOG(P(I)))**0.33333
        20      CONTINUE
                OPEN (2, FILE='CRYNDER', STATUS='NEW')
                OPEN (3, FILE='PLATE', STATUS='NEW')
                WRITE (2,*) 'RADIUS (NM): DV/DR (ML/NM): SURFACE AREA (M2)'
                WRITE (3,*) 'WIDTH (NM): DV/DR (ML/NM): SURFACE AREA (M2)'
                DO 30 I=IMAX, 2, −1
                RM=(RK(I)+RK (I−1)+T(I)+T(I−1))/2.0
                TM=(T(I)+T(I−1))/2.0
                DT=T(I)−T(I−1)
                A=((RM−TM)/RM)**2.0
                B=SSC−2.0*3.141592*TM*LL*1.0E−9
                V=((AM(I)−AM(I−1))*(1.0E−6)−DT*B*1.0E−9)/A
                DV=(V*1.0E+6)/DT
                S=2.0*V/(RM*1.0E−9)
                L=S/(2.0*3.141592*RM*1.0E−9)
                SSC=SSC+S
                LL=LL+L
                WRITE (2,*) RM,DV,SSC
                LM=RK(I)+RK(I=1)+T(I)+T(I−1)
                A=(LM−2.0*T(I−1)
                V=((AM(I)−AM(I−1))*(1.0E−6)−DT*SSP*1.0E−9)/A
                S=2.0*V/(LM*1.0E−9)
                SSP=SSP+S
                DV=V*1.0E+6/DT
                WRITE (3,*) LM,DV,SSP
        30      CONTINUE
                CLOSE (2, STATUS='KEEP')
                CLOSE (3, STATUS='KEEP')
                WRITE (*,*) ''
                WRITE (*,*) 'PORE SIZE DISTRIBUTION WAS OUTPUTTED INTO
                +CRYNDER AND PLATE FILE'
        101     FORMAT (A50)
                END
```

molecule and two parallel graphitic planes can be expressed by [80]:

$$\Phi_{GR}(z)$$

$$=\frac{3}{\sqrt{10}}\epsilon_{GR}\left\{\frac{2}{15}\left[\left(\frac{\sigma_{sf}}{H/z+z}\right)^9+\left(\frac{\sigma_{sf}}{H/z-z}\right)^9\right]\right.$$

$$\left.-\left[\left(\frac{\sigma_{sf}}{H/z+z}\right)^3+\left(\frac{\sigma_{sf}}{H/z-z}\right)^3\right]\right\} \quad (4)$$

Here ϵ_{GR} is the minimum interaction energy of a N_2 molecule with a graphitic surface. The nuclei of the two parallel micrographites are a distance H apart, the molecule being a distance z from the central plane of the two surfaces. These coordinates are illustrated in Fig. 9. Then we can calculate the interaction energy of a N_2 molecule with the micrographitic micropore wall. Kaneko et al. calculated more rigorously the interaction potential of a N_2 molecule in graphite slit pores in the configurations of N_2 normal and parallel to the surface [81]. They used the Steele 10-4-3 potential ϕ_{sf}, Eq. (5) [82], for the interaction energy between a N_2 molecule and a single graphite surface instead of the function by Everett and Powl,

$$\phi_{sf}(z)=2\pi\rho_s\epsilon_{sf}\sigma_{sf}^2\Delta\{(2/5)(\sigma_{sf}/z)^{10}-(\sigma_{sf}/z)^4$$

$$-\sigma_{sf}^4/[3\Delta(0.61\Delta+z)^3]\} \quad (5)$$
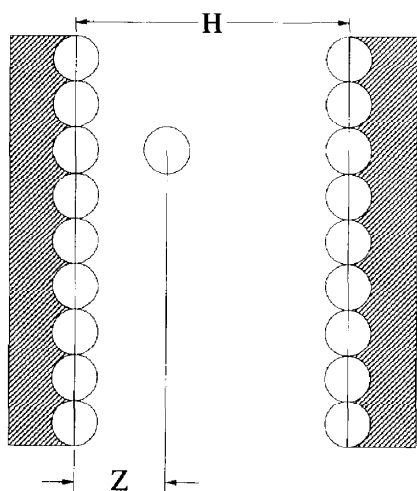
where Δ is the distance between the graphite lay-

ers ($=0.335$ nm), ρ_s is the number of carbon atoms per unit area in a graphite layer ($=114$ nm^{-2}). The 10-4-3 potential is obtained by summation of the Lennnard-Jones potential between a gas molecule and each carbon atom of the individual graphite planes. The exponents 10 and 4 denote the repulsive and attractive interactions of the molecule with the surface graphite plane, while the exponent 3 results from the summation of the attractive part of the potential over the subsurface layers of the graphite. The calculated potential $\Phi(z)$ was obtained by addition of $\phi_{sf}(z)$ and $\phi_{sf}(H-z)$. Fig. 10 shows the potential profiles of a N_2 molecule in a slit-shaped graphitic pore as a function of H, calculated by the two center model. The unit of the potential energy in Fig. 10 is the Lennard-Jones parameter for N_2 ($\epsilon_{ff}/k_B=37.8$ K). This profile indicates the preferred parallel orientation of the N_2 molecule. The effective pore width w determined by experiment is nearly equal to $H-0.24$ (nm); in general H is given by [81]:

$$H=w+0.8506\sigma_{sf}-\sigma_{ff} \quad (6)$$
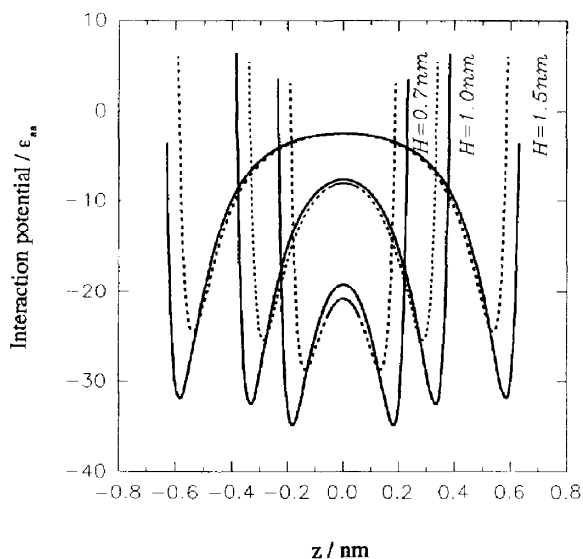
In the micropore system, the potential has deep

Fig. 9. The coordinate of a molecule in a slit-shaped pore.

Fig. 10. Interaction potential profiles for N_2 in a graphite slit pore. (– –) N_2 normal to the surface, (—) N_2 parallel to the surface.

double minima, as shown in Fig. 10; the potential of the whole pore region becomes deeper with a smaller w value. Thus, micropores have a stronger surface field for molecules than the flat or mesoporous surfaces, giving rise to the type I isotherm, that is, enhanced adsorption at the low pressure region. The molecular adsorption in micropores is called micropore filling, which is distinguished from the capillary condensation in mesopores. Although the average potential in micropores shows explicitly the reason for the characteristics of micropore filling, combination of the average potential with the thermodynamic adsorption potential is necessary to get information on the pore size. Furthermore, the adsorbate–adsorbate interaction should be included with the assistance of statistical mechanics.

4.4.2. Thermodynamic description of micropore filling

Molecular adsorption in microporous systems has been described by the thermodynamic Dubinin–Radushkevich (DR) equation [83,84], which is very effective for the determination of the micropore structures. Dubinin assumed that adsorbed molecules have a so-called adsorption potential A, the fractional filling is governed by A, and the micropore size distribution is Gaussian; the DR equation is expressed by

$$W_a/W_o = \exp[-(A/E)^2]$$ (7)

with

$$A = RT\ln(P/P_o) = -\Delta G$$

$$E = \beta E_0$$

where ΔG is the differential free energy of adsorption; W_a is the amount of adsorption at equilibrium pressure P; W_0 is the micropore volume; E_0 and β are the characteristic energy and affinity coefficient (β for N_2 is 0.33). E gives the isosteric heat of adsorption at W_a/W_0 ($=\theta$) = 1/ e by adding the heat of vaporization ΔH_v for the adsorptives [Eq. (8)]. The intercept and slope of the $\ln W$ versus $\ln^2(P/P_0)$ plot leads to the micropore volume and the isosteric heat of adsorption at $\theta = 1/e$ ($=0.4$).

$$q_{st,\theta=1/e} = E + \Delta H_v$$ (8)

The DR equation holds in a variety of adsorption systems. The micropore filling of a system with a distribution of pore sizes can be described by the sum of the contributions from individual pore groups which are characterized by its own pore volume $W_{0,i}$ and E_i (i: group notation). The overall adsorption W_a can be described by the multiterm DR equation [85], as given by

$$W_a = \sum_i W_{0,i}\exp[-(A/E_i)^2]$$ (9)

The DR plot of the high resolution N_2 isotherm is often composed of two or three straight lines. In such a case, the multiterm DR analysis can lead to the pore size distribution, whereas the description by the multiterm DR equation probably comes from the presence of different elementary adsorption processes. Jaroniec and Madey introduced the Γ distribution instead of the Gaussian distribution [86]. Best fitting of an observed adsorption isotherm to the Γ distribution function gives the micropore size distribution. Only the most simple method of determination from the DR analysis is shown here.

4.4.3. Pore size distribution with the Dubinin–Stoeckli relationship

The small angle X-ray scattering by porous media is approximately described by the Guinier equation which is akin to the DR equation. Dubinin noticed its analogy and derived an empirical relationship between the mean pore half-width χ_0 (nm) and the characteristic adsorption energy E_0 (kJ/mol) for carbonous materials with slit-shaped micropores, which is termed the Dubinin–Stoeckli (DS) relation [87]. The simple DS relation is shown in Eq. (10). A constant value of 10 or 12 is used for χ_0 (the constant 10 is more appropriate for other experimental results on the effective pore width w ($=2\chi_0$) [88,89]).

$$\chi_0 E_0 = \text{constant}$$ (10)

McEnaney showed that χ_0 can be expressed by a more complicate function of E_0 [90]. The DS relation is often used for transformation of E_0 to the pore half-width. A Gaussian distribution of

the adsorption potential is assumed in the derivation of the DR equation, and the Gaussian distribution of the pore width of slit-shaped micropores is given by

$$dW_a/d\chi = [W_0/(\delta(2\pi)^{1/2})] \qquad (11)$$

$$\times \exp[-(\chi_0-\chi)^2/2\delta^2]$$

where δ is the dispersion of the distribution and χ is the half-width. W_0 and χ_0 can be determined experimentally and δ is chosen from the best fit with the aid of a personal computer. Then the relationship $dW_a/d\chi$ versus χ, that is, the micropore size distribution, is obtained. The calculation using this method is so easy that it has been widely applied to many carbonous adsorbents, giving a reasonable result. The example of N_2 adsorption on activated carbons at 77 K will be shown in comparison with the results of He adsorption at 4.2 K later.

4.4.4. High resolution α_s plot

The principle of this method is already mentioned above. Firstly this method was developed to determine explicitly the surface area of activated carbons whose apparent BET surface area goes beyond 3000 m^2/g. How the pattern of the high resolution α_s plot is helpful to determine the micropore structure is described below. Activated carbon fiber (ACF) is a newly developed carbonous microporous material, which is not only used for adsorbents and catalysts, but also in electronic devices [91]. ACF has a relatively uniform micropore size distribution compared to conventional granulated activated carbons; mesopores of ACF can be almost neglected. The high resolution N_2 adsorption isotherms of pitch-based ACFs (P20, P25, and P30) are shown in Fig. 11. The ACF samples are obtained by different activation conditions; the order of burn-off is P30 > P25 > P20. These isotherms are not typical type I; they have a linear rise with P/P_0 up to 0.4 without a saturation in the P/P_0 region, becoming almost parallel to the abscissa above 0.4. The linear rise is indicative of presence of considerably larger micropores. Fig. 12 shows the high resolution α_s plot of the N_2 adsorption isotherm for P25. This α_s plot has two swings. As
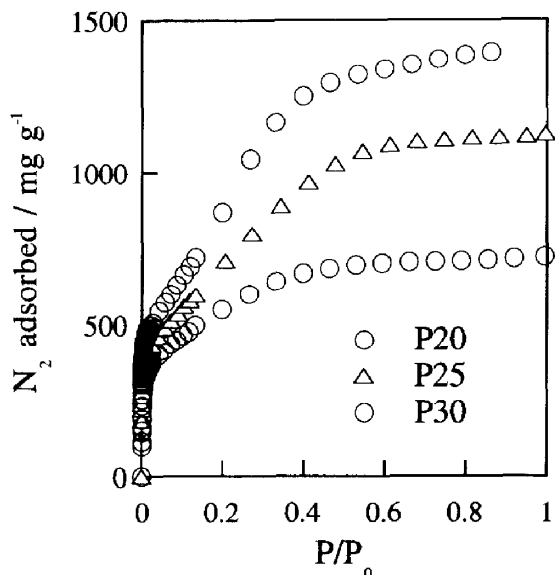

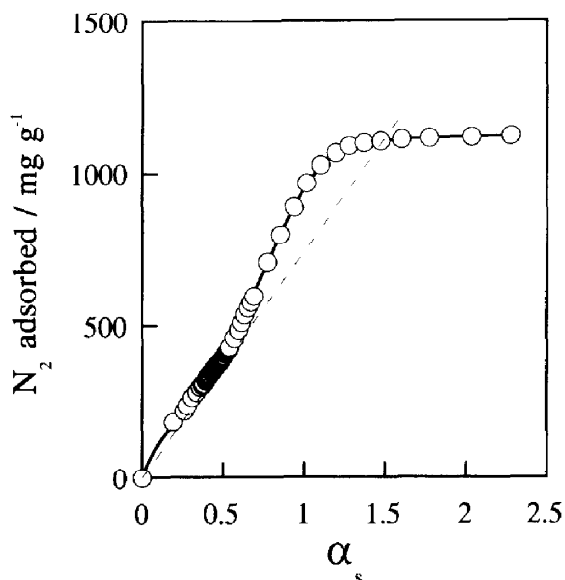Fig. 11. N_2 adsorption isotherms of three pitch-based ACFs (P20, P25, and P30) at 77 K.

Fig. 12. High resolution α_s plot for the N_2 adsorption isotherm of P25.

there is an evident linear region between the two swings and the line can be extended to the origin, the total surface area a_s (m^2/g) is obtained from the relation of $2.05 \times$ slope, when the amount of

adsorption is expressed in mg/g-adsorbent. The extrapolation of the line above $\alpha_s = 1.5$ to the ordinate and its slope lead to the micropore volume W_0 (ml/g) and the external surface area a_{ext} (m²/g). The modified Wicke equation gives an average slit-shaped micropore width w (nm):

$$w = [2W_0/(a_s - a_{ext})] \times 10^3 \qquad (12)$$

The presence of filling and condensation swings suggests both ultra- and supermicropores. Nevertheless, these swings are not yet applied to the determination of the pore size distribution.

4.4.5. He adsorption porosimetry

N_2 molecules are strongly adsorbed at the entrance of micropores due to the quadrupole moment. An H_2O molecule is smaller than a N_2 molecule, but the former has strong preference for the adsorbent because of the dipole moment. A He atom is the smallest spherical monatomic molecule and interacts nonspecifically with any solid surface. He adsorption at 4.2 K is a powerful method for the determination of micropore structures. The He adsorption isotherm at 4.2 K can be determined by gravimetric and volumetric methods. Kaneko et al. used the gravimetric method using a grease-free stainless vacuum line and high precision pressure transducers [88,89,92].

The He adsorption isotherms at 4.2 K can be analyzed by Eq. (11) with $\beta = 0.03$. The He adsorption isotherm at 4.2 K and the N_2 adsorption isotherm at 77 K for cellulose-based ACF are shown in Fig. 13. Here P/P_0 is expressed on a logarithm scale and the amount of adsorption is represented by their volumes using the theoretical adsorbed He density (0.202 g/ml) on a flat surface [93] and the liquid N_2 density (0.807 g/ml), respectively. The amount of He adsorption is much greater than that of N_2 in the low P/P_0 region. This is caused by better accessibility and accelerated bilayer adsorption. Both adsorption isotherms provide different pore size distributions, as shown in Fig. 14. The micropore size distribution from He shifts to a smaller value compared to that from N_2.

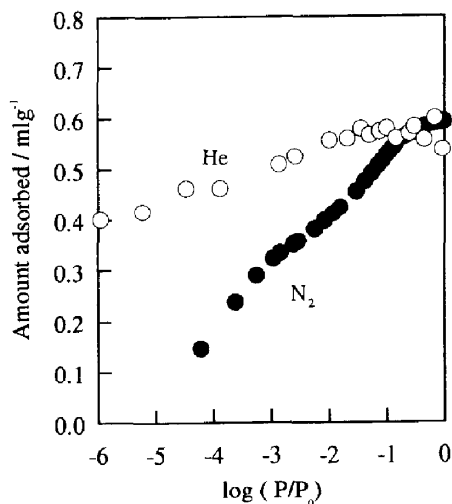Steele [93] showed that the interaction of the second He layer with the graphite surface is very

Fig. 13. The adsorption isotherms of He at 4.2 K and N_2 at 77 K for cellulose-based ACF.
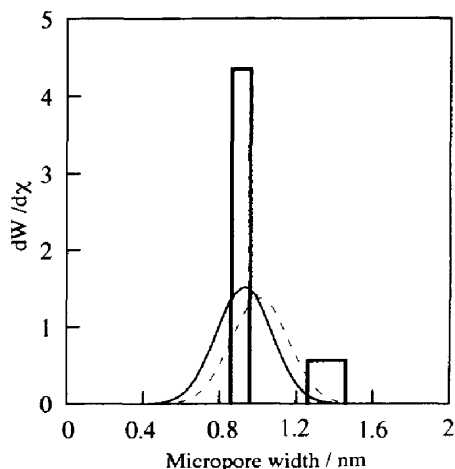

Fig. 14. The micropore size distributions of cellulose-based ACF from (–) from He adsorption at 4.2 K and (——) from N_2 adsorption at 77 K, Bar charts: From the partition analysis using Eq. (13).

important at 4.2 K and the second layer adsorption is accelerated. In the micropore filling process, the second layer adsorption is affected by the micropore field even for the N_2 adsorption. Then, the adsorption mechanism for He on the flat surface can be applied to the analysis of the

micropore filling. Steele extended the Dole equation having no lateral interaction to the description of the He adsorption isotherm on the flat surface to obtain [93].

$$\phi = \frac{\left\{1+c_2\times\dfrac{2-x}{(1-x)^2}\right\}c_1 x}{1+c_1 x+\dfrac{c_1 c_2 x^2}{1-x}} \qquad (13)$$

where θ is the coverage given by the ratio of the amount of adsorption W_a to the monolayer capacity W_m ($\theta = W_a/W_m$) and $x = P/P_0$. c_1 and c_2 are expressed by Eqs. (14) and (15) with the aid of the molecular partition function j_i of a molecule in the ith ($i=1$ or 2) adsorbed layer, the energy difference ϵ_n of an adsorbed molecule and a molecule in the gas, and the potential energy of an atom in the bulk liquid ϵ_{liq}.

$$c_1 = (j_1/j_{liq})\exp[-(\epsilon_1-\epsilon_{liq})/kT] \qquad (14)$$

$$c_2 = (j_2/j_{liq})\exp[-(\epsilon_2-\epsilon_{liq})/kT] \qquad (15)$$

Here c_1 equals to the well-known BET c value. As the interaction of the second adsorbed He layer with the surface is taken into account, c_2 is necessary for the Steele's treatment. When this approach is applied to the description of micropore filling of He, c_1 and c_2 must be evaluated from the molecular potential profile which varies with the micropore width. Fig. 15 shows the potential profile calculated with the Lennard-Jones poten-
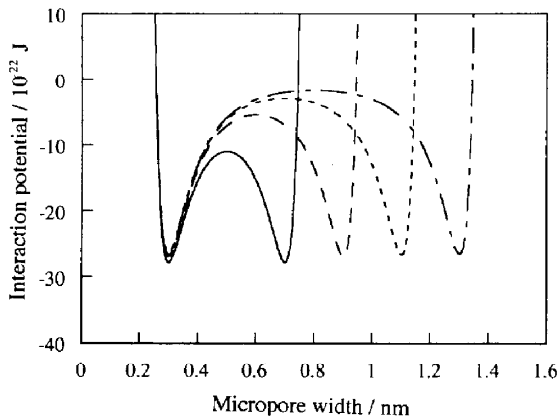
tial for the slit-shaped graphitic micropore as a function of the pore width. The potential depth of the midpoint becomes deeper with a decrease of the pore width. This potential profile leads to both c_1 and c_2 for different pore widths. Hence, we can determine the micropore size distribution by the best fit to the observed adsorption isotherm. Fig. 16 shows such fitting procedure; two kinds of pores having different pore widths are presumed and the fraction was determined by computer fitting. The pore size distribution in the bar chart expression is shown in Fig. 14 together with those from the thermodynamic method. The major distribution almost coincides with the previous distribution by the thermodynamic approach. Consequently, this molecular potential approach supports the effectiveness of the thermodynamic method for the pore size distribution from He adsorption. However, the thermodynamic method using the DS relation cannot be applied to porous systems other than activated carbons. On the contrary, the molecular potential method is available for a general system.

4.4.6. Combined method of average micropore field and adsorption potential

The micropore field is expressed in terms of the Lennard-Jones potential, as already mentioned above. Hill proposed an expression for the adsorption potential by the average molecular

Fig. 15. The interaction potential profiles of He in a graphite slit pore as a function of the pore width.
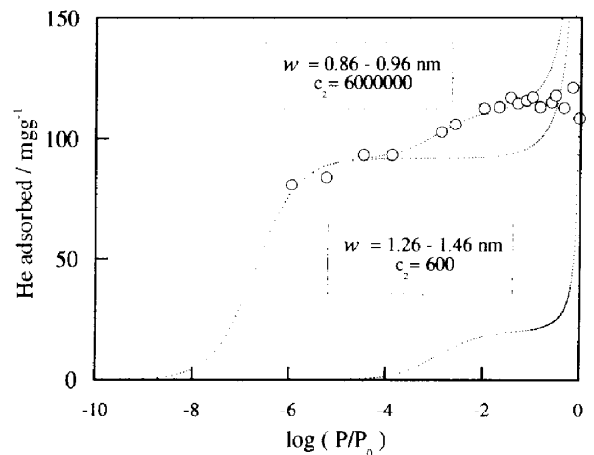

Fig. 16. Partition of He adsorption to pores having different widths.

potentials [94]. Horvath and Kawazoe developed this idea for the slit-pore system in order to evaluate the micropore size distribution [95]. They used two infinite graphite layers for the model. The exponent in their formula is larger than that described above by one. The former potential is calculated for two semi-infinite graphitic slabs, which is more realistic. The potential $\Phi(z)$ between the two graphite layers at the position of z is expressed by

$$\Phi(z) = \frac{\text{constant}}{2\sigma_{sf}^4}\left[\left(\frac{\sigma_{sf}}{H/2-z}\right)^4 + \left(\frac{\sigma_{sf}}{H/2-z}\right)^{10}\right.$$
$$\left. -\left(\frac{\sigma_{sf}}{H/2+z}\right)^4 - \left(\frac{\sigma_{sf}}{H/2+z}\right)^{10}\right] \quad (16)$$

In order to average this potential over the whole pore, the potential is integrated from ξ to $(H-\zeta)$. Here, 2ζ is the sum of the diameter of an adsorbent atom and the diameter of the adsorbate molecule. The integrated potential is assumed to be equal to the adsorption potential A. The relative pressure is related to the average molecular potential as follows:

$$RT\ln(P/P_0) = \frac{\text{constant}}{\sigma_{sf}^4(H-2\zeta)}$$
$$\times\left[\frac{\sigma_{sf}^4}{3(H-\zeta)^3} - \frac{\sigma_{sf}^{10}}{9(H-\zeta)^9} - \frac{\sigma_{sf}^4}{3\zeta^3} + \frac{\sigma_{sf}^{10}}{9\zeta^9}\right] \quad (17)$$

Here the constant includes the polarizabilities and magnetic susceptibilities of the adsorbate molecule and adsorbent atom. The final expression for the N_2/slit-shaped graphite pore is expressed by Eq. (18), where H is in nm.

$$\ln(P/P_0) = \frac{62.38}{H-0.64}\left[\frac{1.895\times10^{-3}}{(H-0.32)^3}\right. \quad (18)$$
$$\left. -\frac{2.709\times10^{-7}}{(H-0.32)^9} - 0.05014\right]$$

Accordingly, we can express each amount of adsorption at a relative pressure in terms of H, which provides directly the pore size distribution, i.e., $w = H - 2r_C$ (r_C is the carbon atom radius). This approach has been used for the determination of the micropore size distribution. Although this is much better than the method us-

ing the capillary condensation theory, we need a more improved method.

This average potential approach can be extended to the evaluation of the cylindrical micropore size distribution. Saito and Foley developed an analytical equation for Ar adsorption isotherms at 87 K for the zeolite group containing VPI-5 and AlPO$_4$ [96]. They used the cylindrical potential of Everett and Powl [79]. When molecules have two degrees of freedom to move across the pore, the adsorption potential is expressed as a function of the pore radius r_{Np} which is the radius of the cylinder at the nuclear position, as given by Eq. (19); the pore radius r_p is determined by subtraction of the radius of the oxide ion, 0.138 nm (in this case the pore wall is composed of oxide ions).

$$\ln(P/P_0) = 36.48\sum_{k=0}^{\infty}\left[\frac{1}{k+1}\left(1-\frac{0.306}{r_{Np}}\right)^{2k}\right.$$
$$\times\left\{\frac{21}{32}\alpha_k\left(\frac{0.306}{r_{Np}}\right)^{10} - \beta_k\left(\frac{0.306}{r_{Np}}\right)^4\right\}\right] \quad (19)$$

where the expansion coefficients α_k and β_k are expressed by

$$\alpha_k = \left(\frac{-4.5-k}{k}\right)^2\alpha_{k-1} \quad (20a)$$

$$\beta_k = \left(\frac{-1.5-k}{k}\right)^2\beta_{k-1} \quad (20b)$$

$$\alpha_0 = \beta_0 = 1 \quad (20c)$$

They compared the calculated pore sizes with the X-ray diffraction data and obtained good agreement within 25%.

Also this type of approach is effective for the description of micropore filling of supercritical gases by slit-shaped micropores. The experimental maximum value W_L of high pressure adsorption for a supercritical gas is related to the micropore width through the average micropore field [Eq. (21)] for the slit-shaped carbonous microporous solid, because the amount of high pressure adsorption of a supercritical gas is mainly

governed by the adsorbate–adsorbent interaction potential.

$$RT\ln(W_1/W_0)$$
$$= \frac{6}{\sqrt{10}} N_A \epsilon_{GR} \left(\frac{2\sigma_{sf}}{w+2r_C}\right)^3 - U^{CO} \quad (21)$$

Here W_L and W_0 are the saturated amount of adsorption of the supercritical gas at high pressure and the micropore volume. In this case H is approximated by the sum of $w/2$ and r_C. U^{CO} is the energy of cooperative micropore filling. N_A is the Avogadro constant. This equation describes the intrapore-field dependent micropore filling for supercritical gases. The linearity of the $\ln(W_L/W_0)$ versus $(w+2r_C)^{-3}$ plot is helpful for the determination of the pore width. The good linearity was shown for adsorption of N_2 and CH_4 by ACFs at 303 K up to 10 MPa. These approaches neglect the adsorbate–adsorbate Lennard-Jones interaction which plays an important role [81]. Also calculation of the potential only is not sufficient for elucidation of adsorbed molecules in pores. The following statistical mechanical approach provides a more reasonable analysis.

4.4.7. Molecular simulation porosimetry

The experimental adsorption isotherm measured on a porous solid sample is the aggregate of the isotherms for the individual pores of different sizes. Consequently, the experimental isotherm is the integral of the single pore isotherm multiplied by the pore size distribution, if we neglect the geometrical and chemical heterogeneities in the porous surfaces. For a slit-shaped pore, this can be described as,

$$N(P) = \int_{H_{min}}^{H_{max}} f(H)\rho(P,H)\,dH \quad (22)$$

where $N(P)$ is the amount adsorbed at pressure P, H_{min} and H_{max} are the widths of the smallest and largest pores, $\rho(P,H)$ is the mean density of N_2 at pressure P in a pore of width H. The $N(P)$ versus P relation is just an adsorption isotherm. $f(H)$ is a pore size distribution function, i.e., the

distribution of pore volumes as a function of pore width H. Therefore, all of the heterogeneities of less crystalline porous solids are approximated by the distribution of pore sizes. If $\rho(P,H)$ can be obtained from the molecular statistics, $f(H)$ can be determined by the best fit to the observed experimental isotherm. The width H in $f(H)$ is not the effective pore width w, as mentioned above. In order to derive the molecular density in a pore, statistical approaches to fluids have been used. Seaton et al. applied the mean field theory to calculate $\rho(P,H)$ [49]. The mean field theory is an approximate theory of inhomogeneous fluids in which the interactions between the fluid molecules are divided into a short-range, repulsive part and a long-range, attractive part. Each is treated separately for faster calculation than full molecular simulation. The contribution of the long-range forces to the fluid properties is treated in the mean field approximation, while the effect of the short-range forces is modelled by an equivalent array of hard spheres. There are two approaches to get the short-range forces – the local mean field theory and the nonlocal one, where the former neglects the short-range correlation, but the latter takes it into account. Seaton et al. adopted the local density approach for their calculation. They calculated $\rho(P,H)$ by the above method. How can we determine $f(H)$ from the calculated $\rho(P,H)$ and the experimental adsorption isotherm $N(P)$? It has a mathematical difficulty. They used the following bimodal log-normal distribution which is flexible to represent the various pore size distributions and is zero for all negative pore widths.

$$f(H) = \{V_1/[\sigma_1 H(2\pi)^{1/2}]\}\exp\{-[\log H$$
$$- \mu_1]^2/2\sigma_1^2\} + \{V_2/[\sigma_2 H(2\pi)^{1/2}]\}$$
$$\times \exp\{-[\log H - \mu_2]^2/2\sigma_2^2\} \quad (23)$$

where V_i is the pore volume of the distribution i, and σ_i and μ_i are the parameters defining the distribution shape. These six parameters in Eq. (23) are determined from the best fit to the experimental adsorption isotherm. The limit of H_{min} corresponds to the smallest pore into which the N_2 molecule can enter. On the other hand, the

upper limit of H, H_{max}, is determined by the width of the mesopore which condenses at the highest experimental pressure. This calculation can determine the pore size distribution from micropore to mesopore. In that work the applicability for the pores of less than 1.3 nm was not shown.

Lastoskie et al. extended the above method to the nonlocal mean field theory [97]. The nonlocal mean field theory gives a quantitative accurate description of even ultramicropore structures. They compared the pore size distributions from the local and nonlocal mean field theories as to real adsorption isotherms by activated carbons; the local theory underestimates the pore size distribution compared with the nonlocal theory. As the calculation with the mean field density theory often gives a qualitative agreement rather than quantitative one. The grand canonical ensemble Monte Carlo simulation is also necessary for such an approach [98]. They also got good results. The molecular simulation studies on the pore size distribution have shown a new picture on the adsorption in the wide range of pores from ultramicropores to mesopores. Understanding of micropore filling and capillary condensation proceeds rapidly. In the future the pore connectivity will be taken into account, so that a more elaborated method will be settled, although so far molecular simulation porosimetry is not a popular method.

5. Small angle X-ray scattering

5.1. Average pore geometry determination

Matter scatters X-rays coherently without loss of consistency of phase. The scattering originates from the emission induced by the periodically oscillating electric field vector of the incident X-ray beam; it is the secondary X-ray of the same wavelength λ from each electron in the scattering body that can respond elastically to the incident field. The secondary X-rays scatter in all directions, but interference with X-rays from adjacent scattering centers occurs without changing the phase relationship, so that the particular distribution of scattered intensity observed is a function of the spatial arrangement of the electrons in the irradiated material. In X-ray diffraction the angular region of X-ray scatter below 5° ($2\theta_X < 5°$, θ_X is the incident angle) is commonly called the small angle region of the X-ray diffraction diagram. In this small angle region, two types of scattering phenomena can be observed: (1) sharp maxima due to long-range periodicity in solids and (2) a decrease in intensity with increasing angle in a continuous manner, which is not due to large internal periodic regularities but to the electronic density heterogeneities of the medium. The heterogeneous entity size is in the order of 0.5 to 10^3 nm. This X-ray scattering, the so-called small angle X-ray scattering (SAXS) gives important structural information on pores producing the distinct heterogeneities of the electronic density.

A new SAXS equipment with a position-sensitive proportional counter and a computer analyzer can give reliable scattering patterns in the scattering parameter s ($=4\pi\sin\theta_X/\lambda$) region 0.005 to 1.0 regardless the necessity of slit correction. The SAXS measurements can provide the pore structures through the electronic density discontinuities in adsorbents, catalysts, and minerals without any damage of the specimen. The SAXS method leads to information on both closed and open pores whose sizes are in the range of micropores to macropores.

An important information from SAXS is the electronic radius of gyration of a particle about its electronic center of mass, R_G (an electronic deficient void may be considered for a porous system). From the knowledge of R_G the linear dimensions of many simple geometrical forms can be calculated, if the shape is known. In the case of a spherical particle of radius R, the radius of the sphere is related to R_G by $R_G = (3/5)^{1/2}R$. If the scattering particle is the slit-shaped pore with micropore width w, horizontal cross-sectional slit length l, and pore depth d, R_G is given by:

$$R_G = [(w^2 + l^2 + d^2)/12]^{1/2} \qquad (24)$$

Guinier demonstrated that the scattering curve

should become exponential and the exponent should equal $-s^2R_G^2/3$, as s approaches zero. The Guinier equation is given by [99]:

$$I(s) = I(0)\exp(-R_G^2 s^2/3) \text{ at } s \to 0 \qquad (25)$$

The Guinier approximation is valid for $sR_G < 1$. A linear relationship of $\ln I$ versus s^2 in the low angle region can be often observed, and then the corresponding R_G can be obtained. Fig. 17 shows the Guinier plot of SAXS in the smallest s region for an ACF sample in air at room temperature. There seems to be a linear region, where the requirement of $sR_G < 1$ is satisfied, so that the R_G of the ACF sample is 1.0 nm. Pores in real porous solids are not so isolated that the no-correlation assumption possibly does not hold. Nishikawa et al. showed that not only pores but also micrographites can cause the evident scattering in the simulation study of SAXS of ACF samples [100]. In particular, determination of the scattering entities for a highly porous solid is difficult at this stage. For simplicity we consider that the scattering entities are pores, as usually assumed. Also the scattering entity should be monodisperse for the Guinier approximation regardless the slight nonlinearity. The observed R_G value should be an average value for scattering entities having a distribution to some extent. The analysis by Shull and Roess for a nonlinear system is available [101]. If a Maxwellian distri-
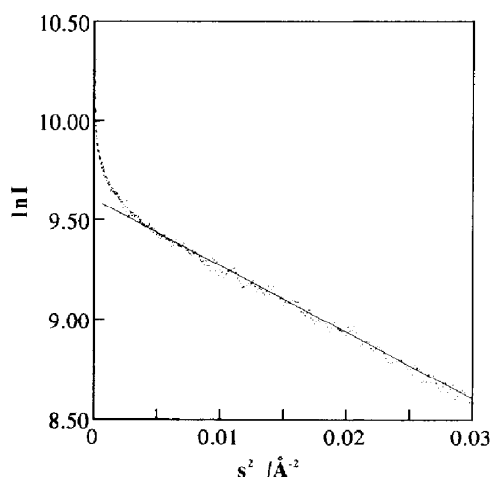
bution is assumed and the Guinier approximation holds for all different pores, the scattering intensity is described by the size distribution $M(R_G)$ having R_G, which can be expressed by:

$$M(R_G) = \{2M_0/r_0^{n+1}\Gamma[(n$$
$$+1)/2]\}R_G^2\exp(-R_G^2/r_0^2) \qquad (26)$$

Here n and r_0 are parameters, and M_0 is the total mass of scattering particles (mass difference for pores). Γ denotes the gamma function. This approximation provides the following expression for the scattering intensity:

$$\log I(s) = \text{constant} - [(n+4)/2]\log(r_0^2/2)$$
$$- [(n+4)/2]\log(s^2+3/r_0^2) \qquad (27)$$

A computer fitting determines n and r_0, and thereby the size distribution is obtained as shown in Fig. 18 for the same sample as in Fig. 17. The size distribution is considerably broad; the mean R_G value can be obtained from the first-order moment using the distribution, so that R_G is 1.5 nm, being significantly different from the 1.0 nm by the simple Guinier analysis.

The R_G value obtained thus provides an average geometrical size of the pore. We presume the slit-shape of the pore of ACF, and thereby R_G is related to the three dimensional parameters w, l, and d through Eq. (24). Further analysis of the scattering at angles higher than the Guinier region also gives information on the shape of the

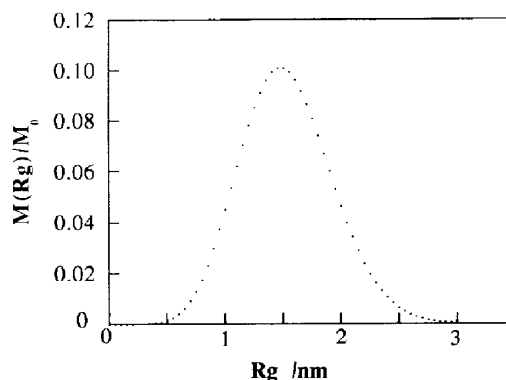Fig. 17. Guinier plot for small angle X-ray scattering of pitch-based ACF.

Fig. 18. The distribution of Guinier gyration radius R_g for pitch-based ACF.

pore. The following thickness plot is available for analysis of the slit-shaped pore.

$$I(s)s^2 = I_t(0)\exp(-R_t^2 s^2) \qquad (28)$$

Here $I_t(0)$ is a constant and R_t is the radius of gyration of thickness. R_t is determined from the linear thickness plot. The thickness plot for the identical ACF sample is shown in Fig. 19. The linearity clarifies the slit-shape of the pore and $R_t = 0.8$ nm is obtained, which is close to the pore width determined by N_2 adsorption. Porod derived thickness and cross section plots for analysis of the SAXS data for thin plates and rod particles, respectively [102]. Approaches other than the Guinier plot should be helpful to elucidate the pore structures regardless the necessity of careful examination. The three dimensional parameters of the slit-shaped micropore in ACF can be determined by these SAXS analyses. The determination of the absolute pore geometry of less-crystalline solids promises further development of understanding of the molecular process in the pores and the materials themselves.

5.2. Latent pore structure determination

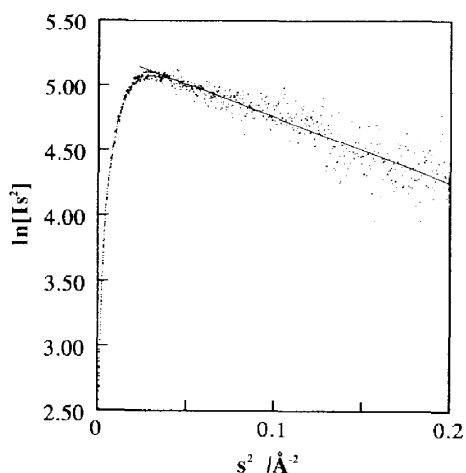Combined examinations of density, N_2 adsorption, and SAXS enable us to evaluate the latent pores separately [45]. The open pore porosity, ϕ_{op}, and closed one, ϕ_{cp}, were described above. In order to separate the closed pores from the total pores, the solid volume fraction ϕ_s ($=\rho_{ap}/\rho_t$), the total porosity (the total pore volume fraction) ϕ_p ($=1-\phi_s$) and the ultrapore porosity ϕ_{up} ($=1-\rho_{ap}[W_0+(1/\rho_{He})]$) must be introduced. Here ρ_t is assumed to be equal to the density from X-ray diffraction examination. Therefore, determination of ρ_t, ρ_{ap}, ρ_{He}, and W_0 gives the above-mentioned porosities. If we determine ρ_{ap}, ϕ_{cp} is obtained. The determination of ρ_{ap} must be carefully done. Not only mercury, but also non-wetting liquid can be used for the measurement. In the case of activated carbon, water is recommended for determination of ρ_{ap} [51].

Debye et al. showed that SAXS analysis can derive the total surface area of the interface originating from the electron density heterogeneity [103]. The specific surface area a_x is associated with porosities ϕ_s and ϕ_p, the apparent density ρ_{ap}, and the correlation length a, as given by:

$$a_x = \frac{4 \times 10^4 \phi_s \phi_p}{a\rho_{ap}} \ (m^2/g) \qquad (29)$$

Here a is related to the correlation function $\gamma(r)$ at a distance r, as described by:

$$\gamma(r) = \exp(-r/a) \qquad (30)$$

a can be determined from Eq. (31) for the slit focus system after Williams [116].

$$I(\tilde{s}) = \frac{A}{(1+a^2 s^2)^{3/2}} \qquad (31)$$

where A is a constant and $I(\tilde{s})$ is the smeared intensity for the slit focus system. The linear Debye–Bueche plot of $I(\tilde{s})^{-2/3}$ versus s^2 leads to a from the slope and intercept:

$$a = \sqrt{\frac{slope}{intercept}} \qquad (32)$$

Then, a_x can be determined by SAXS and density experiments. Fig. 20 shows the Debye plots for pitch-based ACFs. The good linearity is guaranteed in a wide s region and the correlation length was determined, providing the surface area. Fig. 21 compares a_x with a_s (from N_2 ad-

Fig. 19. Thickness plot for the small angle X-ray scattering of pitch-based ACF.
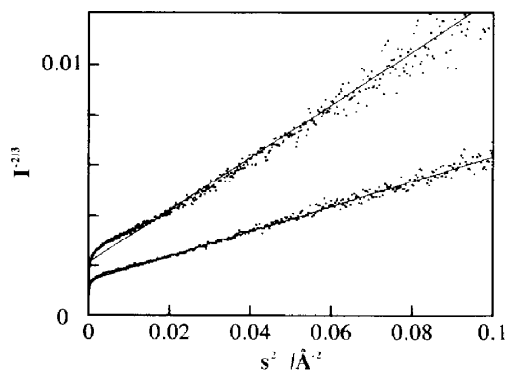
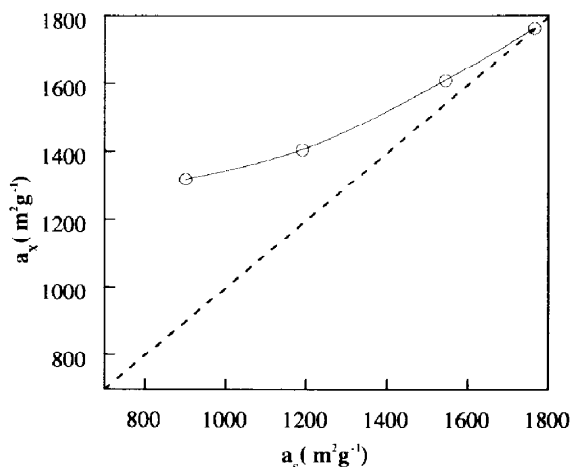Fig. 20. The Debye–Bueche plots for two kinds of pitch-based ACFs.

Fig. 21. Comparison of the surface area a_x from SAXS with a_s from N_2 adsorption.

sorption) for various pitch-based ACF samples with different burn-offs. Almost all a_x values other than that for ACF of the greatest burn-off are greater than the a_s ones; the deviation becomes more predominant with a decrease in the burn-off (or a_s). This difference indicates directly the presence of closed pores and ultrapores (that is, latent pores).

If we assume latent pores of uniform size and shape like a sphere, the number and the size of the latent pores can be estimated from a_x, a_s, ϕ_{up}, ϕ_{cp}, and ϕ_p. When the number concentrations and pore sizes for open pores and latent pores are expressed by n_{op} and n_{lp}, and l_{op} and l_{lp}, respectively, with the assumption of spherical- or cu-

bic-shaped pores, Eqs. (33) and (34) are obtained.

$$\frac{n_{lp}}{n_{lp} + n_{op}} = \frac{(\xi - 1)^2}{(\xi - 1)^2 + (\eta - 1)^3} \quad (33)$$

$$\frac{l_{lp}}{l_{op}} = \frac{\eta - 1}{\xi - 1} \quad (34)$$

Here ξ and η are calculated from observable quantities as follows.

$$\frac{\phi_{up} + \phi_{cp}}{\phi_p} = \frac{n_{lp} l_{lp}^3}{n_{op} l_{op}^3 + n_{lp} l_{lp}^3} = \frac{1}{\xi} \quad (35)$$

$$\frac{a_x - a_s}{a_x} = \frac{n_{lp} l_{lp}^2}{n_{op} l_{op}^2 + n_{lp} l_{lp}^2} = \frac{1}{\eta} \quad (36)$$

Consequently, even in the case of latent pores, we can estimate their number and size; if l_{op} is approximated by the observed pore width w, l_{lp} is obtained. The pitch-based ACF having the smallest surface area has many latent pores (60%) and their size should be ~0.4 nm, which agrees with the molecular adsorption behavior. This latent pore characterization method is also applicable to other important materials.

6. Mercury porosimetry

Mercury intrusion into pores requires application of high pressure to liquid mercury, which is governed by the Young–Laplace equation. The pressure difference ΔP between the pressure P_{Hg} in the mercury and P_g in the gas phase can be described by the surface tension γ_{Hg} of mercury and the mean radius r_m of the curvature of the meniscus.

$$\Delta P = P_{Hg} - P_g = -2\gamma_{Hg}/r_m \quad (37)$$

If the pore is a cylindrical one of radius rp and the contact angle of mercury on the solid surface is θc, rm = rp cosθc and the Washburn equation is obtained.

$$r_p = -(2\gamma_{Hg} \cos\theta_c)/\Delta P \quad (38)$$

Therefore, we can determine the pore volume (pore size) by the extent of mercury penetration as a function of the applied pressure. In an ordi-

nary case the assumption by Ritter and Drake has been used, i.e., γ_{Hg} is 480 mN/m^2 and θ_c is 140° [104]. Of course the contact angle depends on the physical and chemical states of the solid surfaces and the surface tension should change according to the atmosphere. Nonetheless, the assumption by Ritter and Drake is believed to be reasonable. The valid pore range for mercury porosimetry is ~3.5 to 1000 nm, while the molecular resolution porosimetry can only be applied to micropores or mesopores less than 30 nm.

Hysteresis in mercury porosimetry provides information on the complex pore structure such as the throat at the interconnectivity [105]. The pore size distribution $dW(r_p)/dr_p$ is related to the surface fractal dimension D_a by Pfeifer and Avnir [106]:

$$dW(r_p)/dr_p \propto r_p^{2-D_a} \qquad (39)$$

Here $W(r_p)$ is the pore volume of pores having a pore radius r_p. A linear log-log plot of dW/dr_p versus r_p provides D_a which is in the range of 2 to 3. Hence, mercury porosimetry can determine the pore size distribution and the surface roughness at the same time; good linearity in a wide range of pore radii gives detailed information on the pore structures [107].

Even mercury porosimetry which is believed to be a well-established method has been studied from fundamental aspects. Deformation or fracture occurrence in porous specimen due to application of high pressure, discrepancy from N_2 adsorption results, and effect of the interconnectivity must be clarified in future studies.

7. Nuclear magnetic resonance

The strength of the local magnetic field acting on a given nuclear spin in matter is slightly different from that of the external field. The electron cloud surrounding a nucleus induces a shield effect, shifting the observed resonance line. This effect is the so-called chemical shift. The chemical shift of nuclear magnetic resonance (NMR) comes from such interaction. The highly sensitive chemical shift of NMR has contributed to

the elucidation of complex organic molecular structures. The cause for the chemical shift is not necessarily in the molecule, but in the surroundings. In particular, molecules in a confined solid space such as a micropore or a mesopore are affected by the electronic states of the surroundings.

Ito and Fraissard introduced NMR to correlate the chemical shift with the pore width of zeolites using a ^{129}Xe probe (nuclear spin $I=1/2$) [108]. The atomic size of Xe is 0.44 nm and its cross-sectional area is ~0.195 nm^2. Furthermore, Xe near room temperature is a supercritical gas, and thereby it is a good probe for the micropore which is just fit for the Xe atom. Briefly speaking, a narrow Xe NMR signal due to the uniform pore geometry is observed; the chemical shift increases with a decrease in the pore size and increasing the Xe pressure in the pore leads to an increase in the chemical shift due to the Xe–Xe interaction. Although the chemical shift is mainly governed by the electronic microenvironment, other physical processes such as collisions of Xe atoms with each other or the solid wall and the presence of additional atoms in the pores can affect the chemical shift. Fraissard and Ito observed a clear relationship between the chemical shift and the pore size, when the chemical shift extrapolated to zero Xe concentration was used to subtract the increment due to the Xe–Xe interaction.

Conner et al. tried to apply this NMR method to characterize mesoporous silicas [109]. They observed a chemical shift of similar order to that of zeolites despite of the smaller amount of Xe adsorbed by an order of magnitude. The signal is also narrow. However, the dependence of the chemical shift on the Xe adsorbed for silicas is completely different from that for zeolites. That is, it slightly decreases with the adsorbed Xe. They analyzed the observed chemical shift by:

$$\delta_{obs} = x_{ads}\langle \delta_{ads} \rangle + x_{pore}\langle \delta_{pore} \rangle \qquad (40)$$

They expressed the observed chemical shift of Xe, δ_{obs}, by the sum of the average contribution of adsorbed Xe, $\langle \delta_{ads} \rangle$, and interporous Xe, $\langle \delta_{pore} \rangle$. Here x_{ads} and x_{pore} are the fractional concentrations of the adsorbed and interporous Xe, respectively. Thus, the NMR behavior of Xe

atoms in mesoporous silicas are assumed to be caused by the adsorption of the Xe atom on very small pore site (the micropore size) and rapid exchange between Xe in the micropore and Xe adsorbed on the surface. They also examined the NMR signal change for mixing two kinds of mesoporous silicas and showed two distinct signals due to different pore sizes. Consequently, the NMR method is effective for direct checking the heterogeneity of the pore structures. The detection of the chemical shift can become a powerful method in the future, although the determination is still qualitative.

If there is a macroscopic orientation in the solid samples, another NMR principle is helpful to elucidate the pore structure. An electric quadrupole occurs only for spins with quantum numbers $I > 1/2$. Deuterium has a spin quantum number of 1, then the interaction between the nucleus and the electric field shifts the energy level. One observes two resonance lines [Eq. (42)] for hydrocarbons whose principal axis z is given by the direction of the C–D bond so that the xx component of the electric field gradient tensor, $\mathbf{V}_{xx}$, equals the yy component, $\mathbf{V}_{yy}$.

$$\omega = \omega_0 \pm (\omega_Q/2)(3\cos^2\theta_m - 1) \tag{41}$$

Here ω_Q is called the quadrupole frequency, which is given by:

$$\omega_Q = (3\pi/2)e^2qQ/h \tag{42}$$

where Q is the quadrupole moment, $eq = \mathbf{V}_{zz}$ is the zz component of the electric field gradient tensor, and θ_m represents the orientation of the magnetic field on the principal axis of the electric field gradient. Different orientations and motional states of molecules having a C–D bond provide characteristic line shapes. Deuterated benzene provides important information, as benzene has been widely used as a probe adsorptive. Recently Fukasawa et al. applied this D NMR technique to the analysis of adsorbed molecular states in slit-shaped micropores of boehmite microcrystalline aggregates; they determined the orientational angle of a benzene molecule against the micropore wall and the change of the motional state with fractional filling [110]. Hence, D NMR should give infor-

mation on the shape and size of micropores, the pore orientation, and also the density of adsorbed molecules. Further progress in D NMR is expected to contribute to the pore assessment.

8. Thermoporosimetry for wet porous solids

The above-mentioned methods cannot be applied to wet porous systems except SAXS. However, there are many flexible interparticle pore systems in nature and materials. The depression of the melting point of solids in pores is well known, which is explained by the Kelvin equation [111]. Quinson et al. applied this phenomenon to a new porosimetry for wet porous solids such as wet gels [112,113]. They used the dependence of the solidification temperature of the liquid produced in the pores on the pore width. Here, they assume that the adsorbed phase is liquid. The depression of the solidification temperature, ΔT, is given by the curvature $2/r_m$. r_m is greater than the pore radius r_p by the thickness t of the strongly adsorbed layer on the pore wall. The volume dW of the pores where the state changes, such as fusion or solidification, is proportional to ΔT. For water, r_m is expressed by:

$$r_m(nm) = -64.67/\Delta T - 0.23 \tag{43}$$

Then, the pore size distribution dW/dr_p is proportional to ΔT^2:

$$dW/dr_p \propto \Delta T^2 \tag{44}$$

Consequently, the depression of the solidification temperature leads to the pore size distribution after determination of the constants and subtraction of the thickness t. The solidification temperature can be measured by a differential scanning calorimeter. If we compare the solidification and fusion thermograms, the information on the pore shape is obtained. Quinson et al. showed that this thermoporosimetry evaluates the porosity of even small pore sizes of several nm in the wet state.

9. Other methods

There are other methods to determine the pore size distribution. The molecular sieve method with the aid of the adsorption rate measurements for multiprobes having different molecular sizes has been used for qualitative determination of the critical micropore size [95]. The pore size from the molecular sieve method is underestimated compared to that from molecular resolution porosimetry [57]. High resolution electron microscopy is also a powerful method [114,115]. In particular, the image analysis of high resolution transmission micrographs by Endo et al [115] should be a hopeful method for the determination of the pore size distribution.

Although the pore size distribution determination and the related characterization of porous solids are quite important, we still need to make many efforts in order to obtain qualitative methods for each pore system. This review summarizes the main methods for the determination of the pore size distribution and a detailed description on the recent progress in the microporous solid system is given.

Acknowledgments

References

[1] K. Kaneko, Anomalous micropore filling of NO on α-FeOOH-dispersed activated carbon fibers, Langmuir, 3 (1987) 357.
[2] K. Kaneko, N. Fukuzaki and S. Ozeki, The concentrated NO dimer in micropores above room temperature, J. Chem. Phys., 87 (1987) 776.
[3] J. Imai, M. Souma, S. Ozeki, T. Suzuki and K. Kaneko, Reaction of dimerized NO_x ($x=1$ or 2) with SO_2 in a restricted slit-shaped micropore space, J. Phys. Chem., 95 (1991) 9955.
[4] Z.M. Wang, T. Suzuki, N. Uekawa, K. Asakura and K. Kaneko, Mixed valence oxide-dispersion induced micropore filling of supercritical NO, J. Phys. Chem., 96 (1992) 10917.
[5] J. Imai and K. Kaneko, N_2 formation from NO over metal oxide-dispersed microporous carbon fibers, Catal. Lett., 20 (1993) 133.
[6] H. Teng and E.M. Suuberg, Chemisorption of nitric oxide on char, J. Phys. Chem. 97 (1993) 478.
[7] K.K. Unger, J. Rouquerol, K.S.W. Sing and H. Kral (Eds.), Characterization of Porous Solids, Elsevier, Amsterdam, 1988.
[8] F. Rodriguez-Reinoso, J. Rouquerol, K.S.W. Sing and K.K. Unger (Eds.), Characterization of Porous Solids II, Elsevier, Amsterdam, 1991.
[9] J. Rouquerol, F. Rodriguez-Reinoso, K.S.W. Sing and K.K. Unger (Eds.), Characterization of Porous Solids III, Elsevier, Amsterdam, 1994.
[10] R.M. Barrer, Hydrothermal Chemistry of Zeolites, Academic Press, London, 1982.
[11] M.E. Davis, C. Montes, J. Graces and C. Crowder, A molecular sieve with eighteen-membered rings, Nature, 331 (1988) 698.
[12] R.F. Cracknell, P. Gordon and K.E. Gubbins, Influence of pore geometry on the design of microporous materials for methane storage, J. Phys. Chem., 97 (1993) 494.
[13] W.A. Ackerman, D.M. Smith, J.C. Huling, Y.-W. Kim, J.K. Bailey and C.J. Brinker, Gas/vapor adsorption in imogolite: a microporous tubular aluminosilicate, Langmuir, 9 (1993) 1051.
[14] K.S.W. Sing, D.H. Everett, R.A.W. Haul, L. Moscou, R.A. Pierotti, J. Rouquerol and T. Siemieniewska, Reporting physisorption data for gas/solid systems with special reference to the determination of surface area and porosity, Pure Appl. Chem., 57 (1985) 603.
[15] S.J. Gregg and K.S.W. Sing, Adsorption, Surface Area and Porosity, Academic Press, London, 1982, Chap. 3.
[16] A.W. Adamson, Physical Chemistry of Surfaces, Wiley, New York, NY, 1990, Chap. 16.
[17] A. Keizer, T. Michalski and G. Findenegg, Fluids in pores: experimental and computer simulation studies of multilayer adsorption, pore condensation and critical point shifts, Pure Appl. Chem., 63 (1991) 1495.
[18] N.A. Seaton, Determination of the connectivity of porous solids from nitrogen sorption measurements, Chem. Eng. Sci., 46 (1991) 1895.
[19] V. Mayagoitia, M.J. Cruz and F. Rojas, Mechanistic studies of capillary processes in porous media, J. Chem. Soc. Faraday Trans. 1, 85 (1989) 2017.
[20] A.P. Karnaukhov, The main principles of modelling of porous solids. Models of systems with needle-like particles, in F. Rodriguez-Reinoso, J. Rouquerol, K.S.W. Sing and K.K. Unger (Eds.), Characterization of Porous Solids II, Elsevier, Amsterdam, 1991, p. 105.

[21] R.M. Barrer, Zeolites and Clay Minerals, Academic Press, London, 1978, Chap. 2.

[22] S. Iijima, Helical microtubules of graphitic carbon, Nature, 354 (1991) 56.

[23] H. Uchiyama, K. Kaneko and S. Ozeki, Stepwise NO chemisorption processes on synthetic crysotile asbestos, J. Chem. Soc. Faraday Trans. 1, 85 (1989) 3833.

[24] K. Kaneko and K. Inouye, Adsorption of water on FeOOH as studied by electrical conductivity measurements, Bull. Chem. Soc. Jpn., 52 (1979) 315.

[25] T. Ishikawa and K. Inouye, Evolved gas detection of iron oxyhydroxides, J. Therm. Anal., 10 (1976) 399.

[26] F.G.R. Gimblett, A.A. Rahman and K.S.W. Sing, The origin of porosity in hydrous zirconia gels, J. Colloid Interface Sci., 84 (1981) 337.

[27] F.S. Baker and K.S.W. Sing, Specificity in the adsorption of nitrogen and water on hydroxylated and dehydroxylated silicas, J. Colloid Interface Sci., 55 (1976) 606.

[28] K. Kaneko, H. Isobe, T. Katori, I. Tokunaga, T. Gouda, T. Suzuki, S. Ozeki and K. Okuda, Microporous silica microballoons, Colloid Surf., 74 (1993) 47.

[29] R.C. Bansal, J.-B. Donnet and F. Stoeckli, Active Carbon, Marcel Dekker, New York, NY, 1988.

[30] H. Marsh, Introduction to Carbon Science, Butterworths, London, 1989.

[31] K. Kaneko, C. Ishii, T. Arai and H. Suematsu, Defect-associated microporous nature of C_{60} crystals, J. Phys. Chem., 97 (1993) 6764.

[32] R. Rostovtsev, C. Ishii, T. Arai, H. Suematsu and K. Kaneko, Microporous properties of defect controlled C_{60} crystals, Chem. Phys. Lett., to be submitted.

[33] K. Maeda, F. Mizukami, M. Watanabe, S. Niwa, M. Toba and K. Shimizu, Control with polyethers of pore distribution of alumina by the sol–gel method, Chem. Ind., December (1989) 807.

[34] S. Matsuzaki, M. Taniguchi and M. Sano, Polymerization of benzene occluded in graphite–alkali metal intercalation compounds, Synth. Met., 16 (1986) 343.

[35] T. Enoki, H. Inokuchi and M. Sano, ESR study of the hydrogen–potassium–graphite ternary intercalation compounds, Phys. Rev. B, 37 (1988) 9163.

[36] H. Sakuno, A. Ogawa, N. Akuzawa and Y. Takahashi, Absorption of organic molecules on alkali metal–graphite intercalation compounds, Tanso, (1990) 238.

[37] T.J. Pinnavaia, Intercalated clay catalysts, Science, 220 (1983) 4595.

[38] S. Yamanaka, T. Doi, S. Sako and M. Hattori, High surface area solids obtained by intercalation of iron oxide pillars in montmorillonite, Mat. Res. Bull., 19 (1984) 161.

[39] S. Inagaki, Y. Fukushima and K. Kuroda, Synthesis of highly ordered mesoporous materials from a layered polysilicate, J. Chem. Soc. Chem. Commun., (1993) 680.

[40] R.G. Avery and J.D.F. Ramsay, The sorption of nitrogen in porous compact of silica and zirconia powders, J. Colloid Interface Sci., 42 (1973) 597.

[41] R.W. Pekala, C.T. Alviso, F.M. Kong and S.S. Hulsey, Aerogels derived from multifunctional organic monomers, J. Non-Cryst. Solids, 145 (1992) 90.

[42] M. Kurata, K. Kaneko and K. Inouye, Preparation of porous alunite and its water adsorption, J. Phys. Chem., 88 (1984) 2119.

[43] J. Fukazawa, C.-D. Poon and E.T. Samulski, Deuterium NMR investigation of benzene adsorbed on boehmite glasses, Langmuir, 7 (1991) 1727.

[44] J. Fukazawa, H. Tsutsumi, M. Sato and K. Kaneko, Molecular resolution analysis of boehmite aggregates, Langmuir, in press.

[45] M. Ruike, T. Kasu, N. Setoyama and K. Kaneko, Separated assessment of open and closed porosities of less-crystalline microporous solids from adsorption, density and small angle X-ray scattering, J. Phys. Chem., in press.

[46] H. Marsh, Introduction to Carbon Science, Butterworths, London, 1989, Chap. 5.

[47] Y. Morioka and J. Kobayashi, Simulation of desorption process of capillary condensate from pore network, Nippon Kagaku Kaishi, (1982) 549.

[48] J.C.P. Broekhoff and B.G. Linsen, Studies on pore systems in adsorbents and catalysts, in B.G. Linsen (Ed.), Physical and Chemical Aspects of Adsorbents and Catalysts, Academic Press, London, 1970, p. 4.

[49] N.A. Seaton, J.P.R.B. Walton and N. Quirke, A new analysis method for the determination of the pore size distribution of porous carbons from nitrogen adsorption measurements, Carbon, 27 (1991) 853.

[50] C. Lastoskie and K.E. Gubbins, Private communication.

[51] S.J. Gregg and K.S.W. Sing, Adsorption, Surface Area and Porosity, Academic Press, London, 1982.

[52] J. Garrido, A. Linares-Solano, J.M. Martin-Martinez, M. Molina-Sabio, F. Rodriguez-Reinoso and R. Torregrosa, Use of N_2 vs. CO_2 in the characterization of activated carbons, Langmuir, 3 (1989) 76.

[53] D. Avnir, The Fractal Approach to Heterogeneous Chemistry, Wiley, Chichester, 1989, Chap. 4.

[54] M. Sato, T. Sukegawa, T. Suzuki, S. Hagiwara and K. Kaneko, Surface fractal dimensional change of microporous carbon fibers with partial graphitization, Chem. Phys. Lett., 186 (1991) 526.

[55] P.J.M. Carrot and K.S.W. Sing, Assessment of microporosity, in K.K. Unger, J. Rouquerol, K.S.W. Sing and H. Kral (Eds.), Characterization of Porous Solids, Elsevier, Amsterdam, 1988, p. 77.

[56] K. Kaneko, Molecular resolution analysis of α-FeOOH dispersed activated carbon fibers, Langmuir, 7 (1991) 109.

[57] K. Kakei, S. Ozeki, T. Suzuki and K. Kaneko, Multistage micropore filling mechanism of nitrogen on microporous and micrographitic carbons, J. Chem. Soc. Faraday Trans., 86 (1990) 371.

[58] P.B. Balbuena and K.E. Gubbins, Classification of adsorption behavior: simple fluids in pores of slit-shaped geometry, Fluid Phase Equilib., 76 (1992) 21.

[59] S. Brunauer, P.H. Emmett and E. Teller, Adsorption of gases in multimolecular layers, J. Am. Chem. Soc., 60 (1938) 309.

[60] J.C.P. Broekhoff and B.G. Linsen, Studies on pore systems in adsorbents and catalysts, in B.G. Linsen (Eds.), Physical and Chemical Aspects of Adsorbents and Catalysts, Academic Press, London, 1970, p. 23.

[61] D. Atkinson, A.I. McLeod and K.S.W. Sing, Adsorptive properties of microporous carbons: primary and secondary micropore filling, J. Chim. Phys., 81 (1984) 791.

[62] K.S.W. Sing, The use of physisorption for the characterization of microporous carbons, Carbon, 27 (1989) 5.

[63] K. Kaneko, C. Ishii, M. Ruike and H. Kuwabara, Origin of superhigh surface area and microcrystalline graphitic structures of activated carbons, Carbon, 30 (1992) 1075.

[64] K. Kaneko and C. Ishii, Superhigh surface area determination of microporous solids, Colloid Surf. 67 (1992) 203.

[65] J.C.P. Broekhoff and B.G. Linsen, Studies on pore systems in adsorbents and catalysts, in B.G. Linsen (Ed.), Physical and Chemical Aspects of Adsorbents and Catalysts, Academic Press, London, 1970, Chap. 1.

[66] C.G.V. Burgess, D.H. Everett and S. Nuttall, Adsorption hysteresis in porous materials, Pure Appl. Chem., 61 (1989) 1845.

[67] H. Reichert, U. Muller, K.K. Unger, Y. Grillet, F. Rouquerol, J. Rouquerol and J.P. Coulomb, in F. Rodriguez-Reinoso, J. Rouquerol, K.S.W. Sing and K.K. Unger (Eds.), Characterization of Porous Solids II, Elsevier, Amsterdam, 1991, p. 535.

[68] P.J. Branton, P.G. Hall and K.S.W. Sing, Physisorption of nitrogen and oxygen by MCM-41, a model mesoporous adsorbent, J. Chem. Soc. Chem. Commun., (1993) 1257.

[69] C.T. Kresge, M.E. Leonowicz, W.J. Roth, J.C. Vartuli and J.S. Beck, Ordered mesoporous molecular sieves synthesized by a liquid crystal template mechanism, Nature, 359 (1992) 710.

[70] R.M. Barrer and D.M. MacLeod, Intercalation and sorption by montmorillonite, Trans. Faraday Soc., 50 (1954) 980.

[71] A. Linares-Solano, F. Rodriguez-Reinoso, J.M. Martin-Martinez and J. de D.Lopez-Gonzalez, Adsorption of hydrocarbons on air-reacted activated carbons. II. High and low pressure hysteresis, Adsorp. Sci. Technol., 1 (1984) 317.

[72] S.J. Gregg and K.S.W. Sing, Adsorption, Surface Area and Porosity, Academic Press, London, 1982, p. 159.

[73] E.P. Barrett, L.G. Joyner and P.P. Halenda, The determination of pore volume and area distributions in porous substances. I. Computations from nitrogen isotherms, J. Am. Chem. Soc., 73 (1951) 373.

[74] D. Dollimore and G.R. Heal, An improved method for the calculation of pore size distribution from adsorption data, J. Appl. Chem., 14 (1964) 109.

[75] N. Uekawa, Fortran program for the DH method, Department of Chemistry, Faculty of Science, Chiba University, Chiba, Japan.

[76] Y. Morioka, Department of Industrial Chemistry, Faculty of Engineering, Shizuoka University, Hamamatsu, Shizuoka, Japan; Y. Morioka, The pore size distribution and pore network structures of porous solids, Hyoumen (Surfaces), 30 (1990) 598.

[77] A.V. Neimark, A percolation method for calculating the pore size distribution in materials of intermediate porosity based on the adsorption and desorption isotherms in the hysteresis region, Russ. J. Phys. Chem., 60 (1986) 1045.

[78] H. Liu, L. Zhang and N.A. Seaton, Analysis of sorption hysteresis in mesoporous solids using a pore network model, J. Colloid Interface Sci., 156 (1993) 285.

[79] D.H. Everett and J.C. Powl, Adsorption in slit-like and cylindrical micropores in the Henry's law region, J. Chem. Soc. Faraday Trans. 1, 72 (1976) 619.

[80] K. Kaneko, K. Shimizu and T. Suzuki, Intrapore field-dependent micropore filling of supercritical N_2 in slit-shaped micropores, J. Chem. Phys., 97 (1992) 8705.

[81] K. Kaneko, R. Cracknell and D. Nicholson, Nitrogen adsorption in slit pores at ambient temperatures: comparison of simulation and experiment, Langmuir, in press.

[82] W.A. Steele, The Interaction of Gases with Solid Surfaces, Pergamon, Oxford, 1974.

[83] M.M. Dubinin, The potential theory of adsorption of gases and vapors for adsorbents with energetically nonuniform surfaces, Chem. Rev., 60 (1960) 235.

[84] B. McEnaney, Adsorption and structure in microporous carbons, Carbon, 26 (1988) 267.

[85] M.M. Dubinin, Fundamentals of the theory of adsorption in micropores of carbon adsorbents: characteristics of their adsorption properties and microporous structures, Carbon, 27 (1989) 457.

[86] M. Jaroniec and R. Madey, Physical Adsorption on Hetrogeneous Solids, Elsevier, Amsterdam, 1988, Chap. 8.

[87] M.M. Dubinin and H.F. Stoeckli, Homogeneous and hetrogeneous micropore structures in carbonous adsorbents, J. Colloid Interface Sci.,

[88] N. Setoyama, M. Ruike, T. Kasu, T. Suzuki and K. Kaneko, Surface characterization of microporous solids with He adsorption and small angle X-ray scattering, Langmuir, 9 (1993) 2612.

[89] K. Kaneko, N. Setoyama, T. Suzuki and H. Kuwabara, Ultramicroporosimetry of porous solids by He adsorption, in M. Suzuki (Ed.), Fundamentals of Adsorption, Kodansha, Tokyo, 1993, p. 315.

[90] B. McEnaney, Estimation of the dimensions of micropores in active carbons using the Dubinin–Radushkevich equation, Carbon, 25 (1987) 69.

[91] K. Kuriyama and M.S. Dresselhaus, Long-decay-time photoconductivity in highly disordered carbon fibers, Phys. Rev. B, 44 (1991) 8256.

[92] H. Kuwabara, T. Suzuki and K. Kaneko, Ultramicropores in microporous carbon fibers evidenced by helium adsorption at 4.2 K, J. Chem. Soc. Faraday Trans., 87 (1991) 1915.

[93] W.A. Steele, Concerning a theory of multilayer adsorption, with particular reference to adsorbed helium, J. Chem. Phys., 25 (1956) 819.

[94] T.L. Hill, Theory of physical adsorption, Adv. Catal., 4 (1952) 211.

[95] G. Horvath and K. Kawazoe, Method for the calculation of effective pore size distribution in molecular sieve carbon, J. Chem. Eng. Jpn., 16 (1983) 470.

[96] A. Saito and H. Foley, Curvature and parametric sensitivity in models for adsorption in micropores, AIChE J., 37 (1991) 429.

[97] C. Lastoskie, K.E. Gubbins and N. Quirke, Pore size distribution analysis of microporous carbons: a density functional theory approach, J. Phys. Chem., 97 (1993) 4786.

[98] D. Nicholson and N.G. Parsonage, Computer Simulation and the Statistical Mechanics of Adsorption, Academic Press, London, 1982.

[99] A. Guinier and G. Fournet, Small-Angle Scattering of X-Rays, Wiley, New York, NY, 1955, p. 25.

[100] Y. Fujiwara, K. Nishikawa, T. Iijima and K. Kaneko, Simulation of small-angle X-ray scattering behavior of activated carbon fibers adsorbing water, J. Chem. Soc. Faraday Trans., 87 (1991) 2763.

[101] C.G. Shull and L.C. Roess, X-ray scattering at small angles by finely-divided solids. I. General approximate theory and applications, J. Appl. Phys., 18 (1947) 295.

[102] O. Glatter and O. Kratky, Small Angle X-ray Scattering, Academic Press, London, 1982, p. 17.

[103] P. Debye, H.R. Anderson and H. Brumberger, Scattering by an inhomogeneous solid. II. The correlation function and its application, J. Appl. Phys., 28 (1957) 679.

[104] S.J. Gregg and K.S.W. Sing, Adsorption, Surface Area and Porosity, Academic Press, London, 1982, p. 173.

[105] W.C. Conner, A.M. Lane and A.J. Hoffman, J. Colloid Interface Sci., 100 (1984) 185.

[106] P. Pfeifer and D. Avnir, Chemistry in noninteger dimensions between two and three. I. Fractal theory of heterogeneous surfaces, J. Chem. Phys., 79 (1983) 3558.

[107] D.M. Smith, G.P. Johnson and A.J. Hurd, Structural studies of vapor-phase aggregates via mercury porosimetry, J. Colloid Interface Sci., 135 (1990) 227.

[108] T. Ito and J. Fraissaird, ^{129}Xe nuclear magnetic resonance study of xenon adsorbed on zeolite NaY exchanged with alkali-metal and alkaline-earth cations, J. Chem. Soc. Faraday Trans. 1, 83 (1987) 451.

[109] W.C. Conner, E.L. Weist, T. Ito and J. Fraissard, Characterization of the porous structure of agglomerated microspheres by ^{129}Xe NMR spectroscopy, J. Phys. Chem., 93 (1989) 4138.

[110] J. Fukasawa, K. Kaneko, C.D. Poon and E.T. Samulski, Molecular motion in micropore space by D-NMR, in J. Rouquerol, F. Rodriguez-Reinoso, K.S.W. Sing and K.K. Unger (Eds.), Characterization of Porous Solids III, Elsevier, Amsterdam, 1994, p. 311.

[111] R. Defay, I. Prigogine, A. Bellemans and D.H. Everett, Surface Tension and Adsorption, Longman, London, 1966, p. 251.

[112] J.F. Quinson, J. Dumas and J. Serughetti, Alkoxide silica gel: porous structure by thermoporometry, J. Non-Cryst. Solids, 79 (1986) 397.

[113] C.J.G. van der Grift, P.A. Elberse, J.W. Geus, J.F. Quinson and M. Brun, Preparation of porous copper-on-silica spheres, in A.B. Mersmann an S.E. Scholl (Eds.), Fundamentals of Adsorption, Am. Inst. Chem., New York, NY, 1991, p. 939.

[114] R.W. Innes, J.R. Fryer and H.F. Stoeckli, On the correlation between micropore distribution obtained from molecular probes and from high resolution electron microscopy, Carbon, 27 (1989) 71.

[115] M. Endo, K. Oshida, K. Takeuchi, Y. Sasuda, K. Matsubayashi and M.S. Dresselhaus, Fractal analysis on pore structure for activated carbon fibers, Denshi Jyouhou Tsuushinn Gakkai-shi, 77 (1994) 139.

[116] R.J. Jenkins and P.L. Walker, Jr., Small angle X-ray scattering studies on carbons derived from polyfurfuryl alcohol and polyfurfuryl alcohol–ferrocene copolymers, Carbon, 14 (1976) 7.